A Search for High Redshift Type II Quasars from the SDSS BOSS Survey

Rachael M. Alexandroff

Princeton University Department of Astrophysical Sciences

Peyton Hall, Princeton, NJ 08544, USA

rmalexan@princeton.edu

April 29, 2011

ABSTRACT

Luminous AGN with their central engine obscured by gas and dust are classified as type II quasars. Type II quasars at high redshift are suggested by AGN unification models and would help to account for the cosmic X-ray background as well as further our understanding of supermassive blackhole formation and evolution. To date, most identified type II quasars at high redshift are radio-loud. In this paper we present a sample of 207 type II quasar candidates at redshifts $1.55 < z < 4.22$ from the spectroscopic data of the Sloan Digital Sky Survey -III. All objects presented have C IV Gaussian width less than 900km/s (FWHM $<$ 2100km/s) and exhibit a low continuum level. We describe the selection procedure and then describe the sample's bulk propertites as well as presenting several sample spectra. We also show the composite spectra of several subsets of our sample to better examine broad components noticed in some of our spectra. Further study at different wavelengths would allow for confirmation of true obscuration in our sample.

1. Introduction

1.1. General Introduction

The extremely luminous regions at the center of some galaxies are commonly known as Active Galactic Nuclei (AGN). The first of these objects was identified in 1943 by Carl Seyfert so objects such as this one are now referred to as Seyfert galaxies. Other types of AGN include quasars (the topic of this particular paper) and radio-loud galaxies. Non-stellar explanations are proposed for AGN because their spectra suggest a non-thermal origin. The most significant difference is that the spectral energy density of AGN is consistent over most frequencies and thus is too broad to be from a radiating blackbody such as star. Current theories suggest that their extremely large luminosity ($>10^{48}$ erg/s) is attributable to the accretion of gas onto a supermassive black hole (M $> 10^6 M_\odot$) or "central engine" at the center of the galaxy. The in-falling matter has some amount

of angular momentum that causes it to form an accretion disk around the central black hole rather than falling directly past the event horizon. Viscosity during rotation then converts kinetic energy into heat and radiation. The luminosity of the accretion disk is related to its mass accretion rate by the equation below where L_{disk} is the luminosity of accretion, η is the efficiency of the process and $\dot{M}$ is the mass accretion rate (Bradley W. Carroll (2007)).

$$L_{disk} = \eta \dot{M} c^2 \tag{1}$$

Today we use a unification model to characterize the properties of AGN. The variety of observed properties are the result of differences in orientation, luminosity and obscuration (Norman et al. (2002)). The separation between Seyfert and quasar AGN is due to a difference in luminosity across a variety of wavelengths. Quasars are the more luminous AGN over all wavelengths, while Seyferts are defined at some lower luminosity. For example, low X-ray luminosity objects ($L_X < 10^{37} W$) are characterized as Seyfert galaxies while high X-ray luminosity objects ($L_X > 10^{37} W$) are characterized as quasars (Martínez-Sansigre et al. (2006)). Optical astronomers are use a cut in optical luminosity to distinguish between Seyferts and quasars but, as in the X-ray, this cut is somewhat arbitrary.

Seyferts and quasars can both be further subdivided based on obscuration of the central region. It is postulated that the accretion disk of a SMBH is surrounded by a torus of gas and dust whose existence can make it difficult to view the central region around the SMBH at optical wavelengths. According to the unified model an object is classified as type II if its orientation is such that the dusty torus lies along the line of sight whereas an object is classified as type I if the obscuring torus does not lie along the line of sight (Martínez-Sansigre et al. (2006)). There is some evidence to support our "obscuration" hypothesis thanks to infrared (IR) observations. When objects are viewed in the infrared what is observed is the radiation from heated gas and dust. Type II or obscured objects emit brightly in the IR though they do not emit as brightly in the optical, lending credence to the idea that much of their luminosity is obscured by a torus of hot dust. Thus, we can differentiate type II from type I objects because type II obscured objects have a much higher ratio of $L_{IR}/L_{Optical}$ than do type I unobscured objects. As a consequence of obscuration, Seyfert 1s have narrow forbidden but broad permitted (FWHM up to 10^4 km/s) emission lines while Seyfert 2s have narrow forbidden and narrow permitted (FWHM $\preceq$ 1500 km/s) emission lines (Yesuf (2008)).

Forbidden emission lines are the result of energy level transitions that are not permitted by electric dipole selection. Yet there is a discrete, and very small probability of these transitions occurring spontaneously if the material is of very low density because collisional de-excitations occur more rarely. The most extreme laboratory vacuum cannot replicate these conditions on earth(resulting in the name "forbidden") but in the far less dense regions in the Interstellar Medium (ISM) of galaxies these conditions do occur.

How wide an emission line is depends on its distance from the central region. Orbital velocities of gas decrease at greater distance from the central potential well (including the central

blackhole and the galactic bulge). Gas closer to the central potential well experiences larger velocities translating spectrosopically into the doppler broadening of emission lines. Farther from the central potential well, at lower velocities, there is less doppler broadening and the emission lines remain narrow. This is why forbidden lines which can only exist in low-density regions far from the central region are always narrow and why permitted lines which can exist in high-density regions near the central region are usually broad. As a result type 2 objects have both narrow permitted and forbidden lines because the emission lines we see lie only in the less-dense outer region of the galaxy that is not obscured. Along a similar vein, type 1 objects have broad permitted lines and blue continuum (this power law spectrum is believed to be the result of synchrotron radiation in the accretion disk) because we are able to view the central region without obscuration(Yesuf (2008)).

A large sample of type II quasars, especially at high redshifts, has yet to be identified. Radio-loud type II quasars have been known for decades but their radio-quiet counterparts in the optical, IR and X-ray have been much harder to find. Often, objects identified in the X-ray are found to possess broad components when optical spectra are taken and so only about 20% of X-ray candidates possess the truly narrow emission lines necessary to be designated type II quasars (Zakamska et al. (2003)). In general, there is a discrepancy between the kinds of candidates found using optical and X-ray observations. X-ray observations search up to high redshift in a narrow volume of space and so discover many faint quasars that are difficult to observe for follow-up confirmation at optical wavelengths. Optical surveys tend to cover a wide volume of space in less detail and so catch only the most luminous objects (Zakamska et al. (2003)). Searches of previous Sloan Digital Sky Survey (SDSS) data releases have revealed a large sample of potential type II quasars at redshifts $0.3 < z < 0.83$ (Zakamska et al. (2003)) and Narrow Line Seyfert 1s (NLS1s) at $1.5 < z < 3.8$ suggesting that the SDSS presents the large sample size and defined selection criteria necessary to identify and categorize potentially large numbers of AGN for the study of their bulk properties.

We are interested in being able to develop a picture of the evolution and lifetime of AGN in order to better understand the formation and lifetime of SMBHs and their interaction with intra-galaxy star-formation. One of the important criteria we want to constrain is the fraction of obscured quasars by redshift. At low redshift it appears that the ratio of type I to type II quasars is close to 1:1 (see Reyes et al. (2008)) it will take the identification of a much larger sample of type II quasars at high redshift to do the same for large z. In addition, a quantitative understanding of high redshift quasars would allow us to better understand the accretion history of the universe and study the affects of luminosity on AGN structure (Reyes et al. (2008)). We know that type I quasars were most common at redshifts 2-3 when SMBHs did most of their growing but in order to fully understand the implications of this result for AGN evolution, we also need comparable data for type II quasars. Also, it is thought that high redshift type II quasars contribute a substantial fraction of the cosmic hard x-ray background (Zakamska et al. (2003))

1.2. Review: AGN Emission Lines

Type II quasars are characterized by narrow permitted emission lines without underlying broad components and high-ionization line ratios that indicate nonstellar ionization. It is difficult to set a standard definition for the split between narrow and broad emission lines. In this paper we adopted a cut of C IV gaussian σ width < 1500km/s which translates into C IV FWHM < 3500. This allows for much broader emission lines than the work of Zakamska et al. (2003) which uses a limit of FWHM(Hβ) < 2000km/s or σ width < 850 km/s and certainly much broader than the criterion of Hao et al. (2005) which uses a limit of FWHM(Hβ) < 1200 km/s or σ width < 510 km/s. It is the same as the criteria used in Yesuf (2008).

Ionization line ratios also help to separate and identify different AGN. High-ionization line ratios are the result of photoionization by a power-law continuum indicative of AGN activity and were originally used to separate type II quasars from star-forming galaxies for it is observed that AGN have higher flux ratios of [OIII]/Hβ. Yet Zakamska et al. (2003) also argued that similar criteria could be used to separate NLS1s from type II quasars. Zakamska et al. (2003) used the following criteria to identify type II quasars:

$$\log(\frac{[OIII]\lambda5008}{H\beta}) > \frac{0.61}{\log(\frac{[NII]}{H\alpha}) - 0.47} + 1.19 \tag{2}$$

$$\log(\frac{[OIII]\lambda5008}{H\beta}) > \frac{0.72}{\log(\frac{[SII]}{H\alpha}) - 0.32} + 1.30 \tag{3}$$

and

$$\log(\frac{[OIII]\lambda5008}{H\beta}) > 0.3 \tag{4}$$

These are similar to the criteria used to separate NLS1s from type II quasars; namely that NLS1s exhibit:

$$\log(\frac{[OIII]\lambda5008}{H\beta}) < 3 \tag{5}$$

Unfortunately the relevant emission lines for these diagnostics do not appear in our high-redshift search so we were forced to rely on the width of the CIV emission line for this study.

In this paper we present 207 high redshift ($1.55 < z < 4.22$) type II quasar candidates selected from the new SDSS BOSS survey (pre-release DR9). Section 2 will cover the selection criteria and properties of the sample. Section 3 will present the composite spectra of the sample. Finally, in Section 4 we will provide our conclusions. We assume a flat ΛCDM Cosmology with $\Omega_m = 0.26$, $\Omega_\Lambda = 0.74$ and $h = 0.71$ (Spergel et al. (2007)) throughout this paper.

2. Sample Selection and Data Processing

2.1. Sloan Digital Sky Survey Baryon Oscillation Spectroscopic Survey

The Sloan Digital Sky Survey (SDSS) has been in routine operation since 2000 and the Baryon Oscillation Spectroscopic Survey (BOSS) forms a part of SDSS-III (2008-2014) (Eisenstein et al. (2011)). SDSS uses a dedicated wide field of view, 2.5-meter telescope at Apache Point Observatory in New Mexico with a large mosaic CCD camera and two double spectrographs each fed by 500 optical fibers with $2''$ optical diameter for its operation since the BOSS upgrade. The spectral resolution of the new BOSS spectrographs varies from $\lambda/\Delta\lambda \sim 1300$ at $3600\mathring{A}$ to $\lambda/\Delta\lambda \sim 3000$ at $10{,}000\mathring{A}$ (Eisenstein et al. (2011)). SDSS-III includes four surveys and has three scientific themes: dark energy and cosmological parameters, the history and structure of the Milky Way, and the population of giant planets around other stars (Eisenstein et al. (2011)). The BOSS survey is devoted to the first scientific theme and will attempt to better define the expansion history of the universe using the baryon acoustic oscillation (BAO) feature in large-scale structure as a standard ruler for measuring cosmological distances. To that end, over its lifetime BOSS will measure the redshifts of 1.5 million galaxies and the Lyα forest spectra of 150 000 quasars in order to make extremely accurate measurements (percent-level precision) of the distance-redshift relation $d_A(z)$ and the Hubble parameter $H(z)$. BOSS will cover 10,000 deg^2, and as of the beginning of this research BOSS had already observed 240,000 galaxy spectra and 29,000 high-redshift (z $\geq$ 2.2) quasar spectra (Eisenstein et al. (2011)).

More precise measurements of the distance-redshift relation and Hubble parameter at large distances will aid in our understanding of cosmic acceleration and dark energy by allowing further constraints on the dark energy equation-of-state parameter w and its derivative with respect to redshift w_a as well as better constraints on the Hubble constant H_0 and the curvature parameter $\Omega_k \equiv 1 - \Omega_m - \Omega_{DE} - \Omega_{rad}$ (where Ω_k is the total density parameter if k represents the curvature of the universe, Ω_m is the density of matter, both baryonic and dark, Ω_{DE} is the density of dark energy and Ω_{rad} is the density of radiation). BOSS will make these measurements using BAO because the transverse BAO scale constrains the angular diameter distance and the line-of-sight BAO constrains the Hubble parameter. BAO measurements from SDSS-I/II were made for a redshift of $z \approx 0.275$. BOSS will be the first survey to attempt to detect the BAO feature in the Lyα forest and should be able to measure $d_A(z)$ to within 4.5% and $H(z)$ to within 2.6% assuming 15 quasars per degree^2 over 10, 000 degree^2 at a redshift of $z \approx 2.5$ (Eisenstein et al. (2011)).

Of interest to us is the 1.5×10^5 high-redshift quasar spectra in the process of being gathered for BOSS out of 4×10^5 targets. So many targets are necessary because the target selection algorithm is far from perfect and so the sample tends to suffer from stellar contamination. Targets were selected over a redshift range of $2.2 \leq z \leq 4$ with 40 targets per degree^2 in order to result in the 15 quasar detections per degree^2 needed in order to use Lyα forest absorption within the range of BOSS spectrographs to observe the desired high-redshift structure. While BAO science does not require a homogeneous sample, other quasar science is improved by the existence of such a sample

so 20 of the 40 targets per degree^2 were chosen using a "core" selection method (Eisenstein et al. (2011)). While initially useful for BAO measurements, we will examine the quasar spectra in an attempt to identify type II quasars.

2.2. Faint Images of the Radio Sky at Twenty-cm

The Faint Images of the Radio Sky at Twenty-cm(FIRST) survey operated using the National Radio Astronomy Observatory (NRAO) Very Large Array (VLA) in its B-configuration in Socorro, New Mexico. FIRST data was collected from 1993-2004 with some additional data taken in 2009. The North and South Galactic Cap were both covered and so FIRST covers a similar area to SDSS. Using an automated mapping pipeline, images are produced covering 1.8"/pixel with an rms of 0.15 mJy and a resolution of 5". Measurements of peak and integrated flux are also produced by fitting a two-dimensional Gaussian to each source Yesuf (2008). Approximately 30% of sources so far have counterparts in SDSS. A search of the FIRST catalog was completed with the positions of our type II quasar candidates which returned 8 matches within 1" of the target. The significance of this finding will be discussed in section 2.4.

2.3. Selection Criteria

Objects from the entire BOSS survey to date were included in our initial search. Previous searches of SDSS-I and SDSS-II have looked for type II quasars at redshift $0.3 < z < 0.83$ (see Zakamska et al. (2003)). The cut-off at $z < 0.83$ was to ensure the existence of [OIII] λ 5008 in all spectra for AGN classification (Zakamska et al. (2003)). BOSS data allows us to examine candidates at redshift $z > 1.5$. At this redshift the [OIII] emission line is no longer present so we chose to use the C IV (1549 $\mathring{A}$) line as a potential diagnostic to distinguish objects with broad or narrow lines.

All collected spectra are run through the SDSS BOSS pipeline which produces best fits for the object's redshift and classifies the object as a galaxy, star or quasi-stellar object accordingly. This data is then stored along with the spectra in several FITS files produced by the Princeton-1D code written by Dr. David Schlegel. Of these files, SPZline and SPZbest FITS files were accessed throughout the course of this research. SPZline FITS files contain information such as line width and line area on a selection of emission lines for each object such as Lyα and C IV. SPZbest FITS files contain best fits for a variety of data including redshift.

First, the IDL package *readspec* developed by Dr. Schlegal was used to extract CIV σ line width information from SPZline FITS files. If objects are at a redshift high enough for the C IV emission line to be visible then they are AGN and so our code identified all possible AGN (and any objects incorrectly labelled as AGN by an incorrect redshift determination). The resulting distribution of line widths and redshifts for these AGN are presented in figure 1 and 2 respectively.

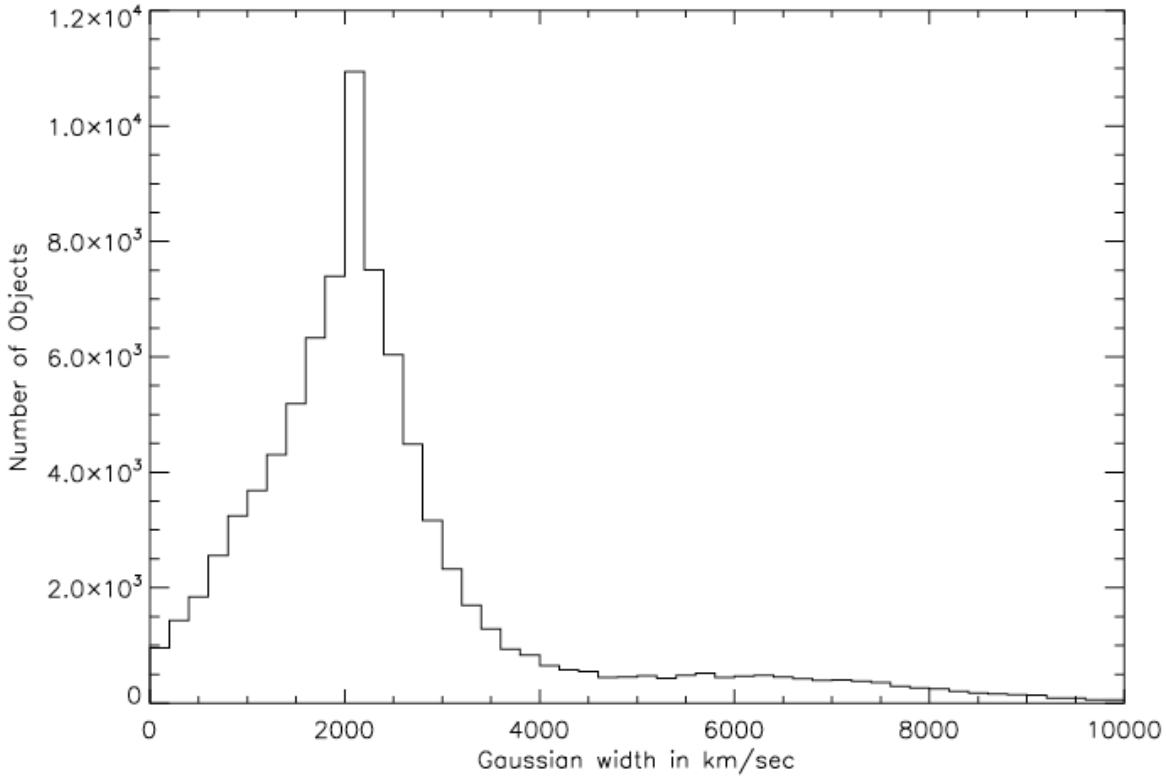

Fig. 1.— The distribution of CIV λ1549 σ width for all AGN in the SDSS BOSS survey. CIV σ width is used as one diagnostic for locating type II quasars. Obscured quasars have narrow permitted emission lines because the broadline region of the quasar is blocked from view by a torus of dust and gas. We will use the condition CIV σ width < 1500 km/s to select candidate objects with narrow permitted emission lines likely to be type II quasars. The distribution of CIV σ widths itself looks Gaussian (except for the narrow tail at high σ width) so our search will focus on the extremely narrow end of the distribution.

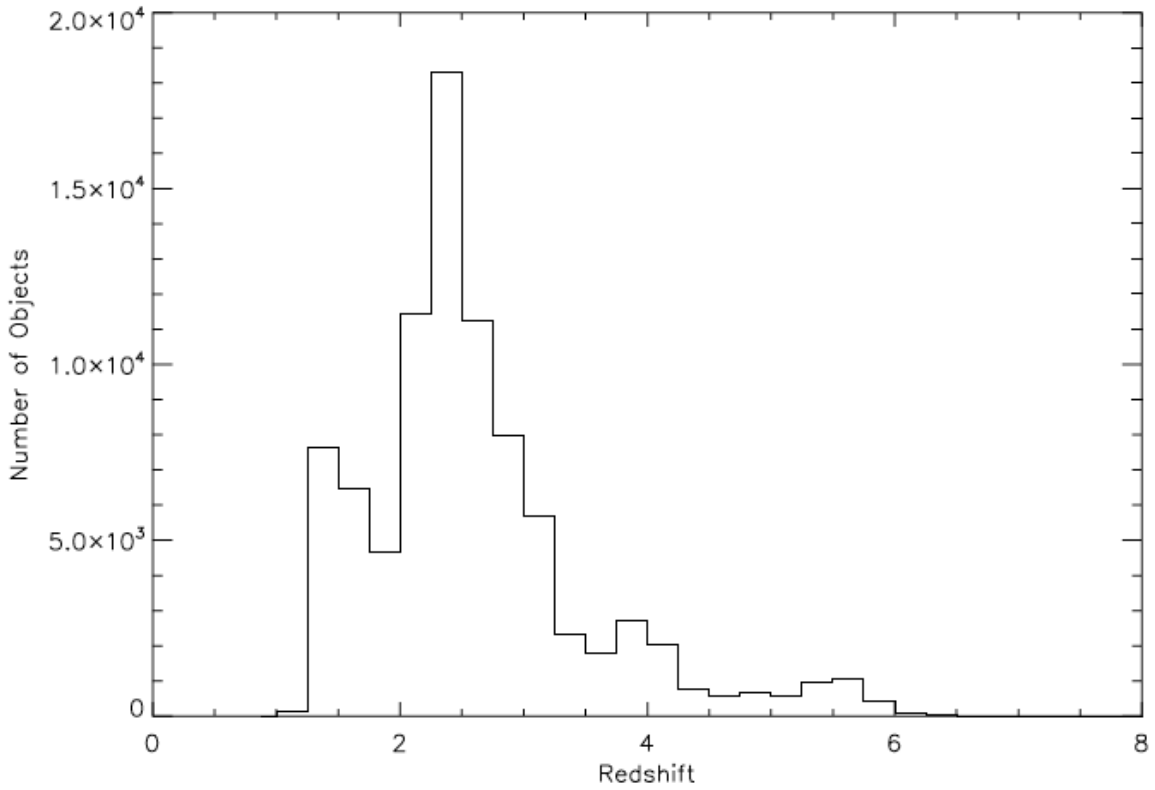

Fig. 2.— The distribution of redshift for all AGN in the SDSS BOSS survey. Redshifts below $z = 1.5$ do not include the CIV emission line in the observable range of the SDSS and so are not part of our sample. A redshift of $z = 6$ represents the farthest observable quasar and so represents the upper cut-off of redshift.

Redshifts below $z = 1.5$ do not include the CIV emission line in the observable range of the SDSS and so are not part of our sample. A redshift of $z = 6$ represents the farthest observable quasar and so represents the upper cut-off of redshift. The distribution of CIV σ widths itself looks Gaussian (except for the narrow tail at high σ width) so we decided to focus our search on the extremely narrow end of the distribution. Our first criteria was to select only objects with CIV σ width <1500km/s to eliminate objects with broad emission lines. In the end due to the search algorithm used and time constraints our samples would have σ line widths no greater than 893 km/s or FWHM no greater than 2100 km/s in line with the work of Zakamska et al. (2003).

Our next step was to eliminate objects with any *zwarning* flag set. The *zwarning* flag is set by the BOSS pipeline and marks spectra with bad redshift fits. Errors include "χ^2 fit is too close to χ^2 for the next best fit" meaning the pipeline couldn't differentiate between its chosen model fit and the next best fit so there is a high probability the fit is incorrect. Another common *zwarning* is "Negative emission in a QSO line" which means an object classified as an AGN has an absorption line which is unphysical and so the pipeline fit must be incorrect. A *zwarning* flag calls into doubt the calculated redshift but the object in question could still be a type II quasar. As a future task these objects might be explored further. The gaussian width and redshift distributions of all AGN that do not have a *zwarning* flag set are shown in figures 3 and 4. In addition, objects with line area < 0 flux-units*Ångstroms were also omitted as this is unphysical or represents an absorption line the pipeline has mistaken for emission that was not flagged with the correct *zwarning*. Finally, to observe the most likely candidates first we combined information on the candidate objects line area and line width. In search for objects with narrow line width but strong emissions (large line area), we first looked at objects with the greatest value of $linearea - linewidth$. This was deemed the best approach to avoid looking at objects where noise was mistaken for a very narrow CIV line because with a large line area the emission would be very narrow but still strong.

Final classification was done by visual inspection. Only the first 930 objects were observed due to time constraints. The sample that was observed can be shown in Figure 5. Of the 930 objects examined, many were not type II quasars. Several were interesting objects outside the scope of this paper (see Section D of the appendix) but the majority of these candidates were instead identified as NLS1 AGN. NLS1s show many similar features to type II AGN such as narrow "broadlines" or optical Balmer lines that would normally be broad in Seyfert 1 objects. Interestingly however, they are not obscured objects as they still exhibit the strong blue continuum of unobscured objects. An example of an identified NLS1 is shown in figure 16. Unlike a type II quasar the continuum level is high and blue (sloping down to the right) and the lines appear relatively broad. Figure 7 shows the luminosity of our candidates compared to the luminosity of those objects we identified as NLS1s. Continuum flux at 1450 Ångstroms were gathered by converting the rest wavelength to emitted wavelength using the equation

$$\lambda_{emitted} = \lambda_{rest} \times (1 + z) \tag{6}$$

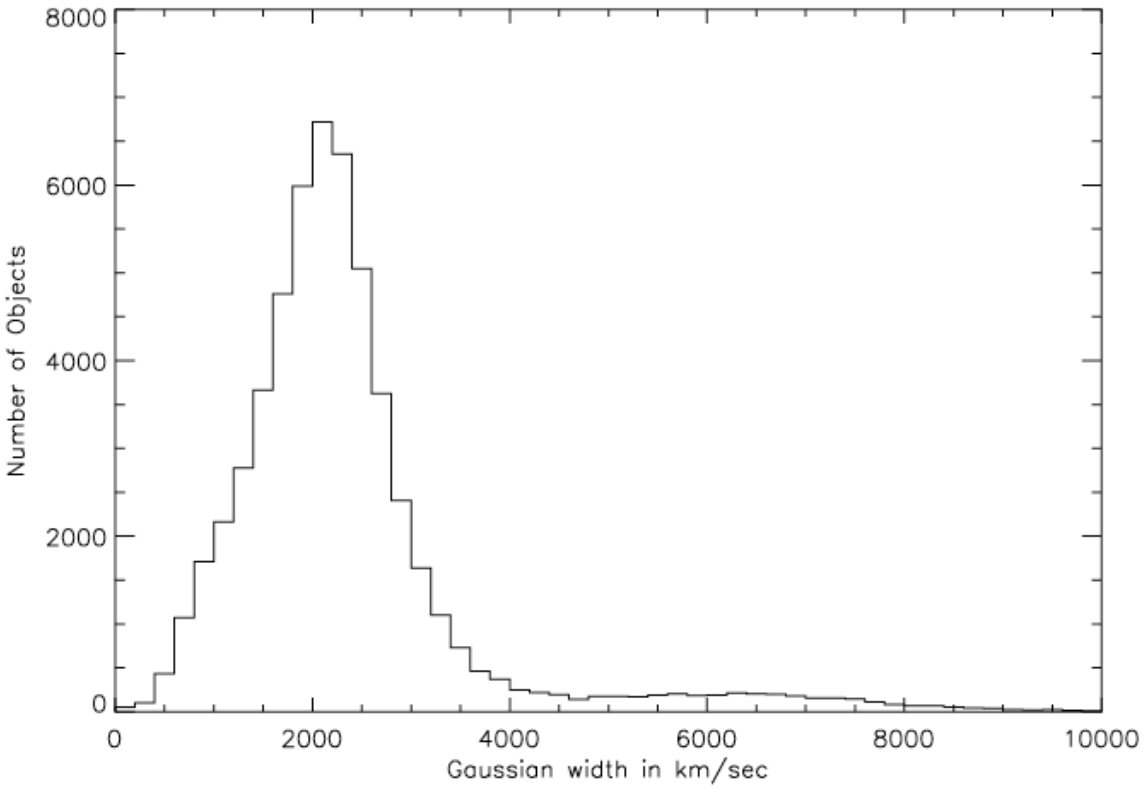

Fig. 3.— The distribution of CIV λ1549 σ width for all AGN in the SDSS BOSS survey excluding objects with a zwarning value that calls into question the accuracy of their redshift determination. Many objects with small CIV σ width were eliminated in this cut making it likely the pipeline attempted to label noise as a very narrow CIV line but the mistake was caught. Some of the eliminated objects may be type II quasars with the wrong redshift. Follow-up visual inspection of these objects might reveal extremely narrow type II quasar candidates.

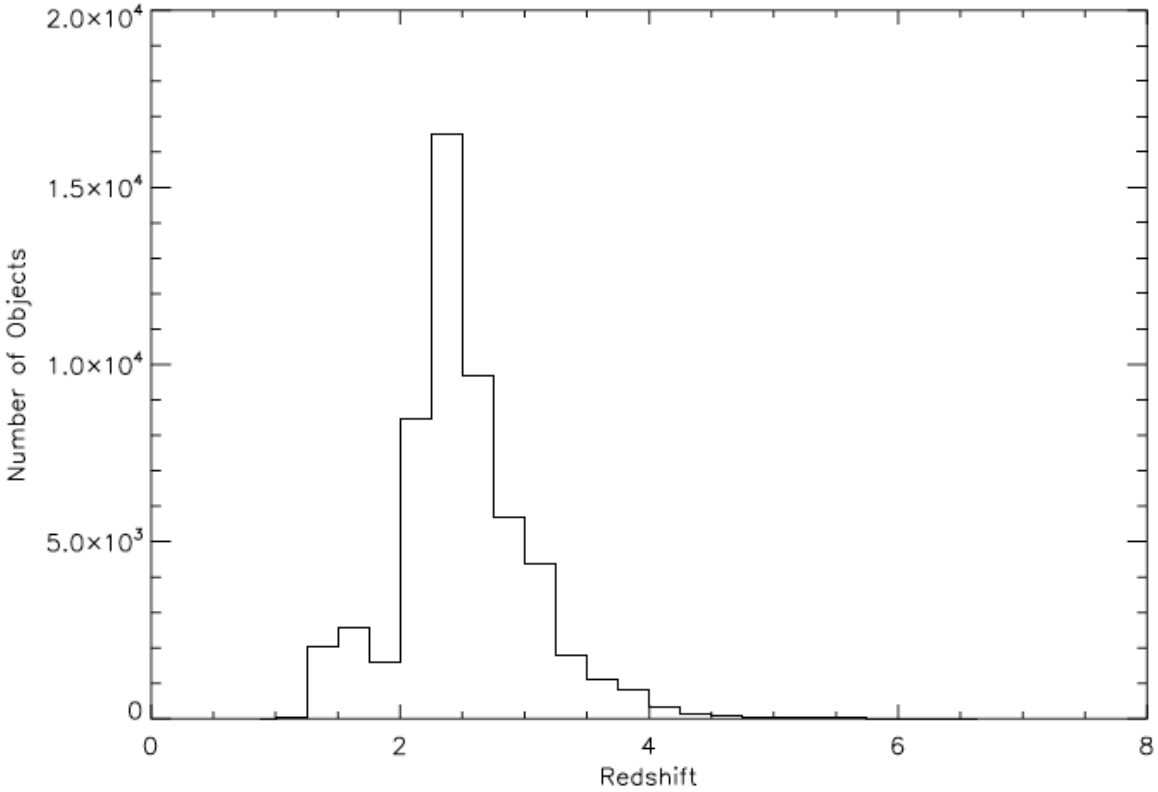

Fig. 4.— The distribution of redshift for all AGN in SDSS BOSS survey excluding objects with a *zwarning* value that calls into question the accuracy of their redshift determination. Many of the objects thought to be at a high redshift were removed at this cut making it likely the pipeline did not correctly determine their redshift. Some of the eliminated objects may still be type II quasars with the wrong redshift.

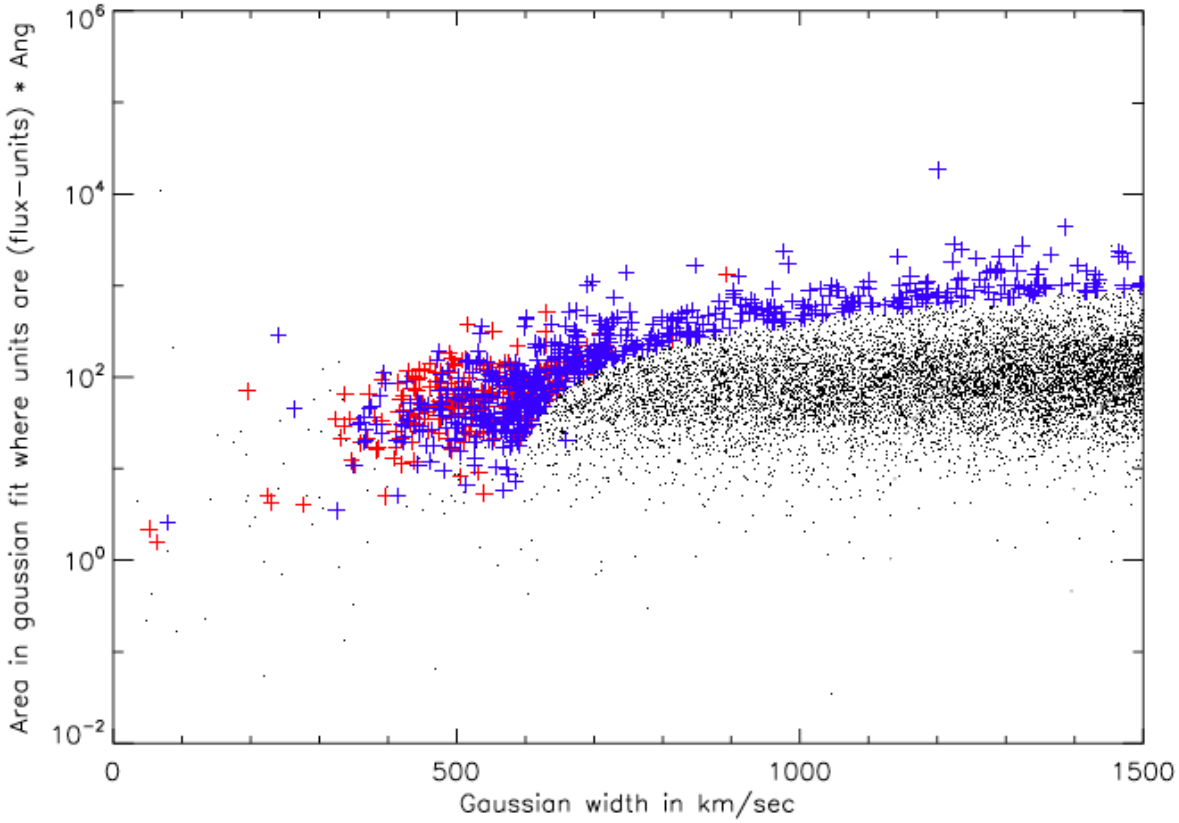

Fig. 5.— The distribution of CIV λ1549 σ width compared to CIV λ1549 line area for all objects in SDSS BOSS survey with CIV σ width < 1500 km/s. All objects in this sample represent potential type II quasar candidates. This distribution was used to determine the order in which objects were visual inspected by looking at objects with the highest value of $linearea - linewidth$ first. Objects in red were visually inspected for classification and were determined to be likely type II quasars. Objects in blue were visually inspected for classification and were determined not to be type II quasars. It is interesting to note that, of the objects inspected, almost no type II quasar candidates were identified below a σ line width of 800km/s suggesting we could have made our line width cut-off smaller and missed few candidates.

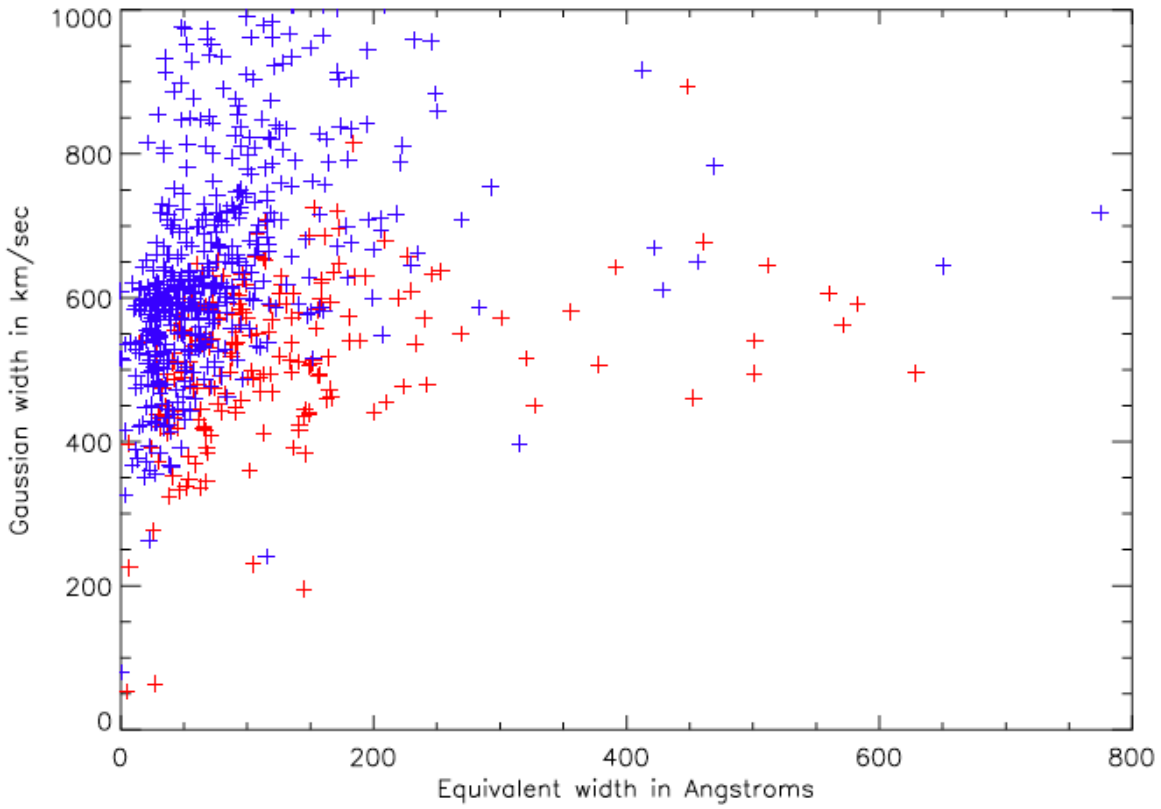

Fig. 6.— Graph of equivalent width (*Å*ngstroms) to CIV (λ1549) σ line width for all objects visually inspected. The equivalent width of an emission line is the ratio of its area to the continuum level. We would expect type II quasars to have greater values of equivalent width than NLS1s as obscured objects have lower continuum levels. Objects in red were visually inspected for classification and were determined to be likely type II quasars. Objects in blue were visually inspected for classification and were determined not to be type II quasars.

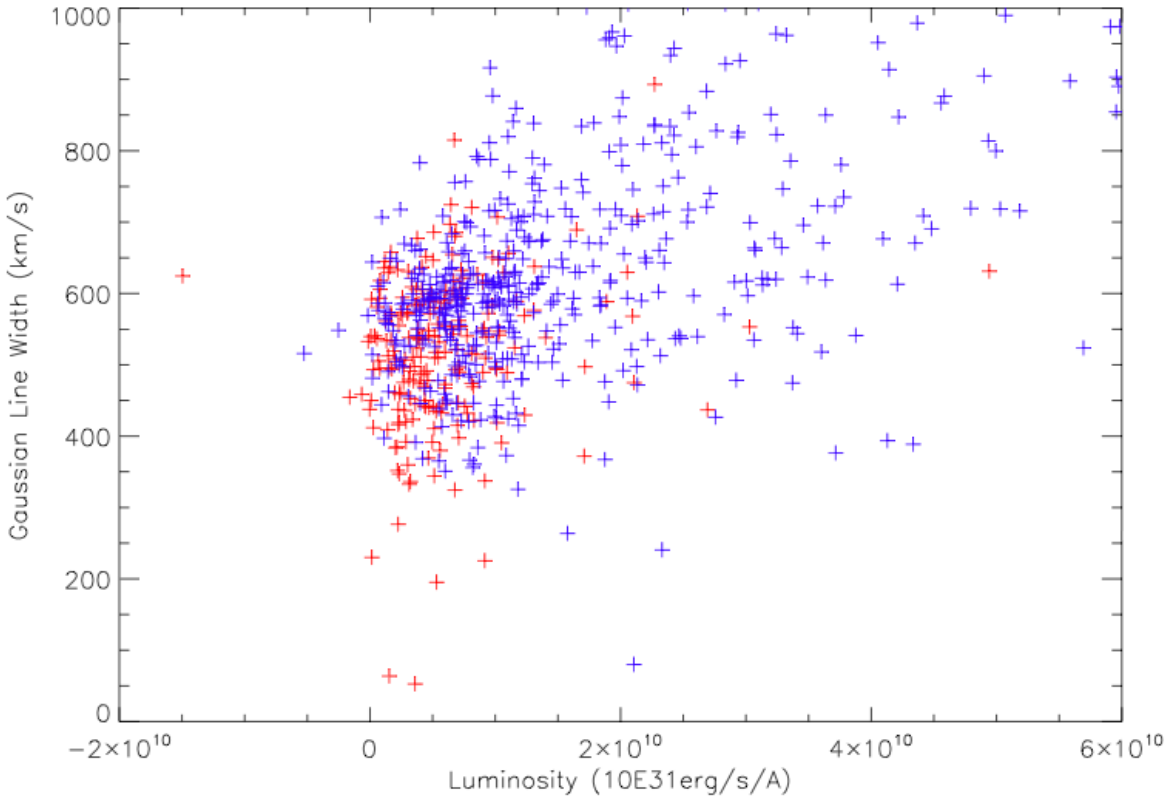

Fig. 7.— Graph of continuum (rest $\lambda = 1450$) luminosity versus CIV (λ1549) σ line width. Because type II quasars have their central engines obscured by a dusty torus we would expect them to have smaller continuum luminosities than NLS1s. Objects in red were visually inspected for classification and were determined to be likely type II quasars. Objects in blue were visually inspected for classification and were determined not to be type II quasars.

and then by averaging the flux at the 5 pixels around the calculated wavelength. To convert from flux to luminosity the formula below was used (see Hogg (1999)).

$$L = 4\pi D_L^2 S \tag{7}$$

Where D_L is the luminosity distance. The luminosity distance was calculated by numerical integration using sm code written by Dr. Michael Strauss and then translated into IDL. As we would expect for obscured objects, our type II quasars had a lower optical luminosity at a continuum wavelength than did the NLS1s. One way to distinguish NLS1s from type II quasars is to observe objects in the mid-Infrared (mid-IR) where dust surrounding an obscured object would radiate. Follow-up observations of candidates in the mid-IR would confirm identification as obscured objects. Our type II quasars will exhibit a much higher ratio of $L_{IR}/L_{optical}$ than unobscured objects such as NLS1s (see Zakamska et al. (2004)).

Strong type II candidates were selected based on a combination of extremely narrow emission lines and low continuum levels. Figure 17 represents an extremely strong candidate type II quasar. The emission lines are extremely narrow while the continuum is extremely low and does not appear blue. Other candidates, while still strong contenders presented some unexpected features. For an example refer to figure 22. While the emission lines in this image are extremely narrow, the candidate exhibits a much broader base which was not identified by the pipeline due to the absorption feature to the left of the emission line. The absorption feature is probably the result of dust in the surrounding galaxy. A broad base such as this does not necessarily mean the object is not a type II quasar. Another possible explanation is that the broad component is light from the central engine that has scattered off dust clouds near the quasar and been reflected along the line of sight. For another example of a strong candidate type II quasar with a broadened base see also figure 21. One way to confirm this hypothesis would be to examine polarimetry of sources with a broad component for scattering off of a nearby cloud should polarize the light (see Zakamska et al. (2005)). Other candidates presented more of a mystery. For examples, see figure 23 and 24. Both of these spectra have the extremely narrow emission lines we would expect of a type II quasar with a broadline region obscured by dust. Yet, both exhibit strong, blue continua that makes it extremely unlikely they are obscured objects. Again, follow-up observations at different wavelengths might enable a final diagnostic to be made.

In the end, 207 candidates were identified that we believe to be strong or possible type II quasars. A list of these objects can be found in table 1 for the 87 strong candidates identified and in table 2 for less certain candidates that display only certain features of type II quasars. The median FWHM of our candidates was 1254 km/s (see 8). While all but one of candidates meets the FWHM cut-off for type II quasars set by Zakamska et al. (2003) of FWHM $<$ 2000 km/s only 43% have a FWHM $<$ 1200 km/s (the criteria of Hao et al. (2005)).

The mean redshift of our sample is 2.72, and 57 of our 207 candidates or 27% have a redshift greater than 3.0 (see figure 9). At lower redshift, line ionization ratios are frequently used to

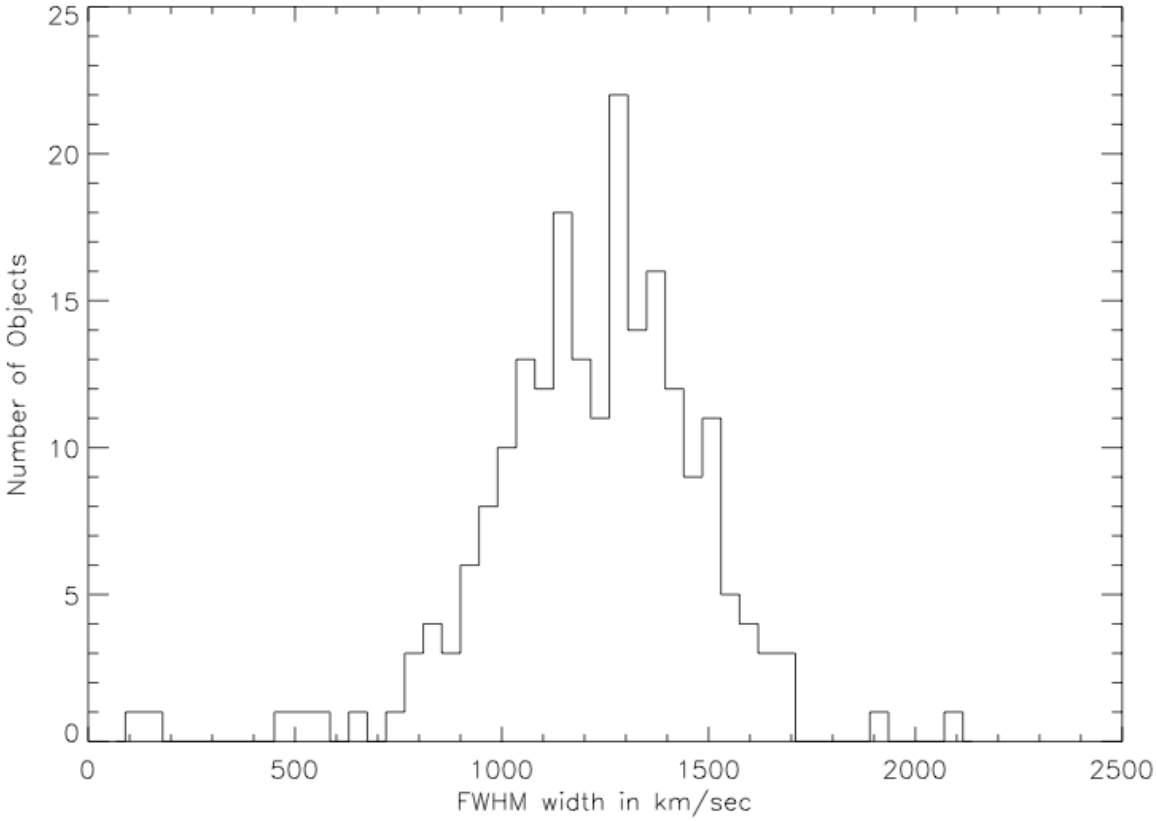

Fig. 8.— Distribution of FWHM for the type 2 quasar candidates identified. 2003AJ....126.2125Z use a FWHM of Hβ <2000 km/s to identify type II quasars. The majority of our objects do meet this criteria. However, only 43% of our objects meet the criteria of Hao et al. (2005) who used a FWHM < 1200 km/s to identify type II quasars.

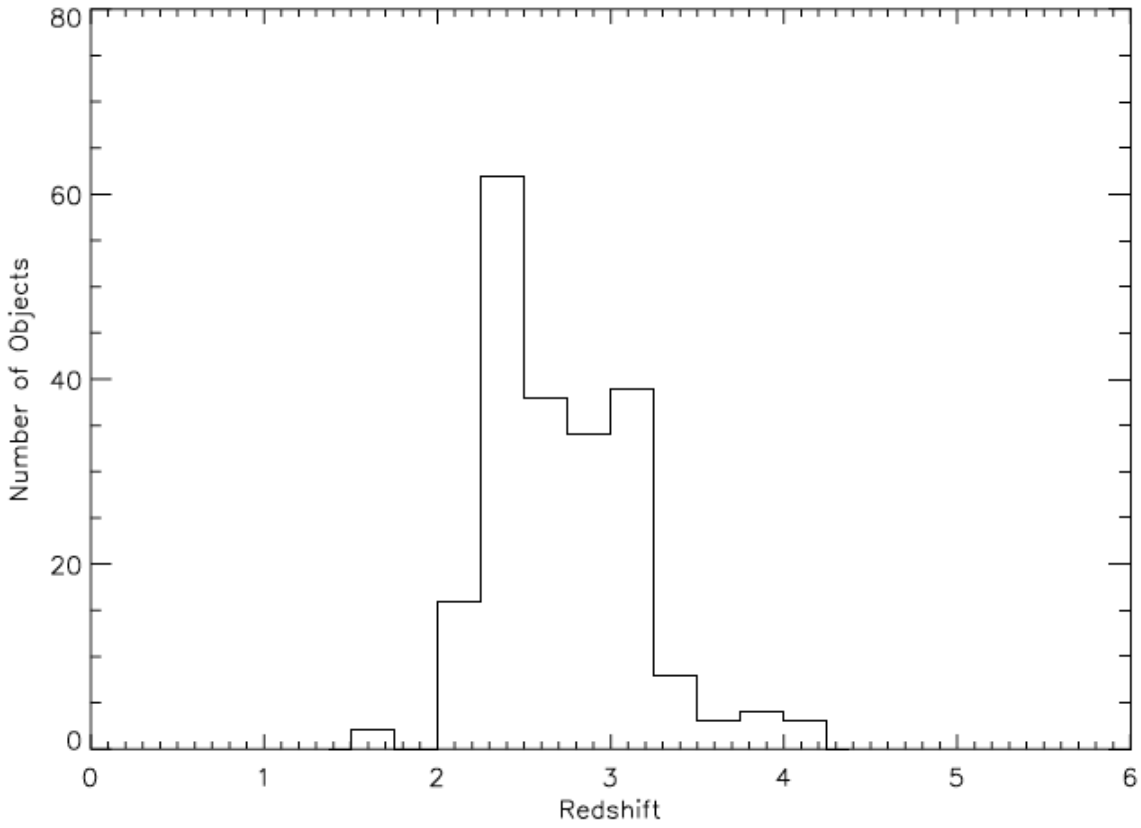

Fig. 9.— Distribution of redshift for the type 2 quasar candidates identified. The mean redshift of our sample is 2.72 and 57 of our type II quasar candidates have a redshift $> z = 3.0$.

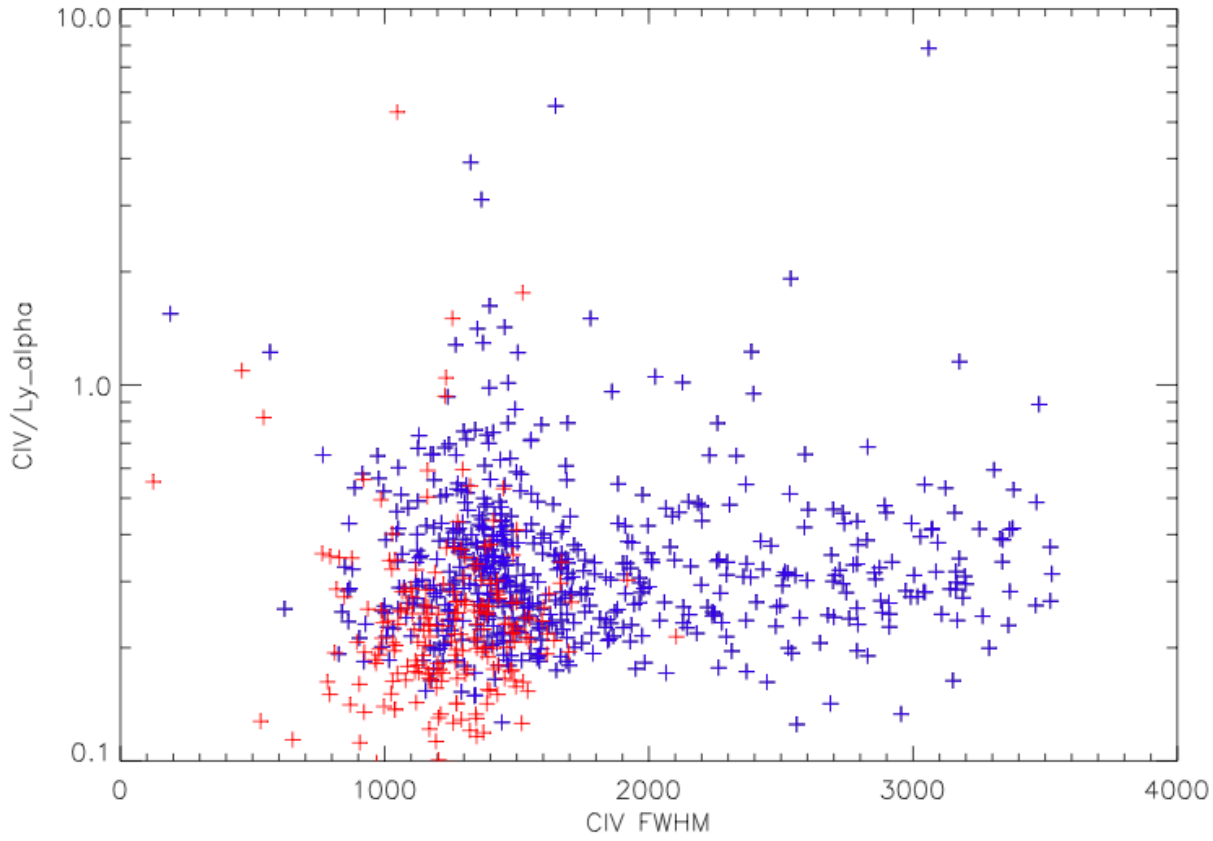

Fig. 10.— Ratio of CIV/Lyα vs FWHM of CIV. All of the emission lines usually used to look for high ionization line ratios in type II quasars are not visible with the SDSS at these redshifts. We sought other line ratios that might be useful in separating type II quasars from NLS1s.

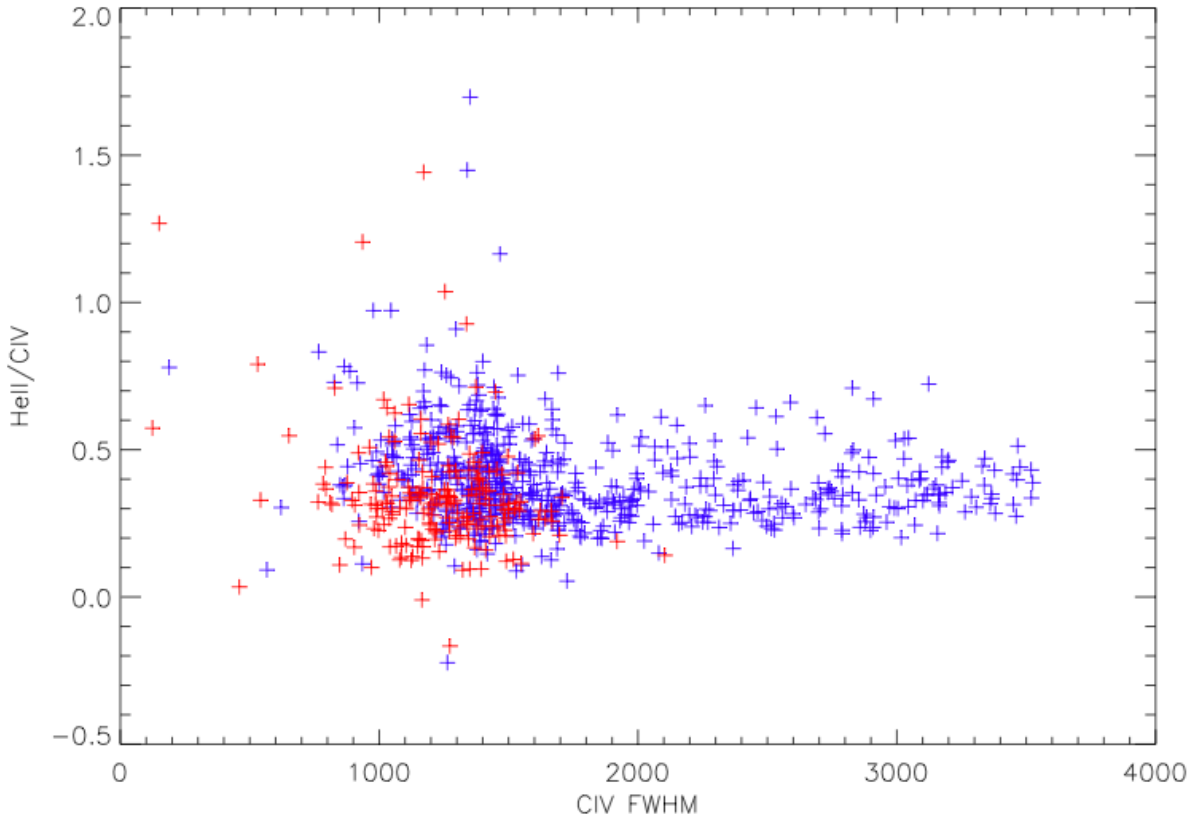

Fig. 11.— Estimate of He II/CIVα cvs. FWHM of CIV. All of the emission lines usually used to look for high ionization line ratios in type II quasars are not visible with the SDSS at these redshifts. We sought other line ratios that might be useful in separating type II quasars from NLS1s.

distinguish types of AGN (see specifically Zakamska et al. (2003) or the brief discussion in section 1.2 of this paper). At the high redshifts examined in this paper, most of these emission lines are not observable by SDSS so in figures 10 and 11 we attempt to examine some available emission line ratios for possible trends. We examined the ratio of CIV to Lyα (figure 10) and the ratio of He II to C IV (figure 11). Fluxes of Lyα, C IV and He II were identified by converting rest wavelengths to emitted wavelengths using equation 6 and then taking the maximum flux within $\pm$ 2 pixels. While in both cases our potential type II candidates appear to exhibit lower line ratios on average, no bimodality appears to be present. These line ratios would likely make poor diagnostics to distinguish type II quasars from NLS1s.

2.4. Radio Property

While a population of high redshift radio-quiet type II quasars has only recently been discovered, a population of high redshift radio-loud type II quasars has existed in the literature for decades. We have found 8 matches within 1" of our type II quasar candidates within the FIRST catalog. This means these 8 sources are not the radio-quiet objects we are hoping to identify but instead represent radio-loud quasars. Radio-loud quasars are an interesting subset of AGN but not the population we are searching for. Several of the identified radio-loud quasars are distinctly doubled (see figure 12) meaning we are seeing lobes from relativistic jets. Interestingly, several of the identified radio sources were not deemed to be strong type II candidates but were instead identified as potential candidates exhibiting only some of the features of a type II quasar.

3. Composite Spectra

This section presents several composite spectra of our candidate type II quasars. Creating composite spectra is a useful technique because it generates spectra with higher signal to noise than a single spectra which enables us to examine weaker emission lines, the continuum (see Yesuf (2008)) and weak broadening features. For this paper spectra were created using the *coadd* macro for supermongo (sm) written by Dr. Michael Strauss. The *coadd* macro first uses spline interpolation to interpolate all spectra to rest wavelengths and then performs the coaddition by averaging the spectra. The results for a variety of subsections of our data are displayed in figures 13, 14, 15. Figure 13 was made by coadding only the spectra of strong candidate type II quasars contained in table 1. Interestingly, while the CIV line appears very narrow in this coadded spectra, the Lyα emission line does appear to have a bit of a broad base. Figure 14 presents the coadded spectra of only those candidates we felt possessed some, though not all of the features of type II quasars (see table 2). In this case the Lyα, C IV and C III emission lines all seem to show some broadening though it looks as though this is tempered by absorption on the bluer side of the emission line. Finally, figure 15 is the coadded spectra of all 209 candidates. Again, we see a bit of broadening on all three lines though less so than for figure 14. Due to the higher signal to noise ratio the final

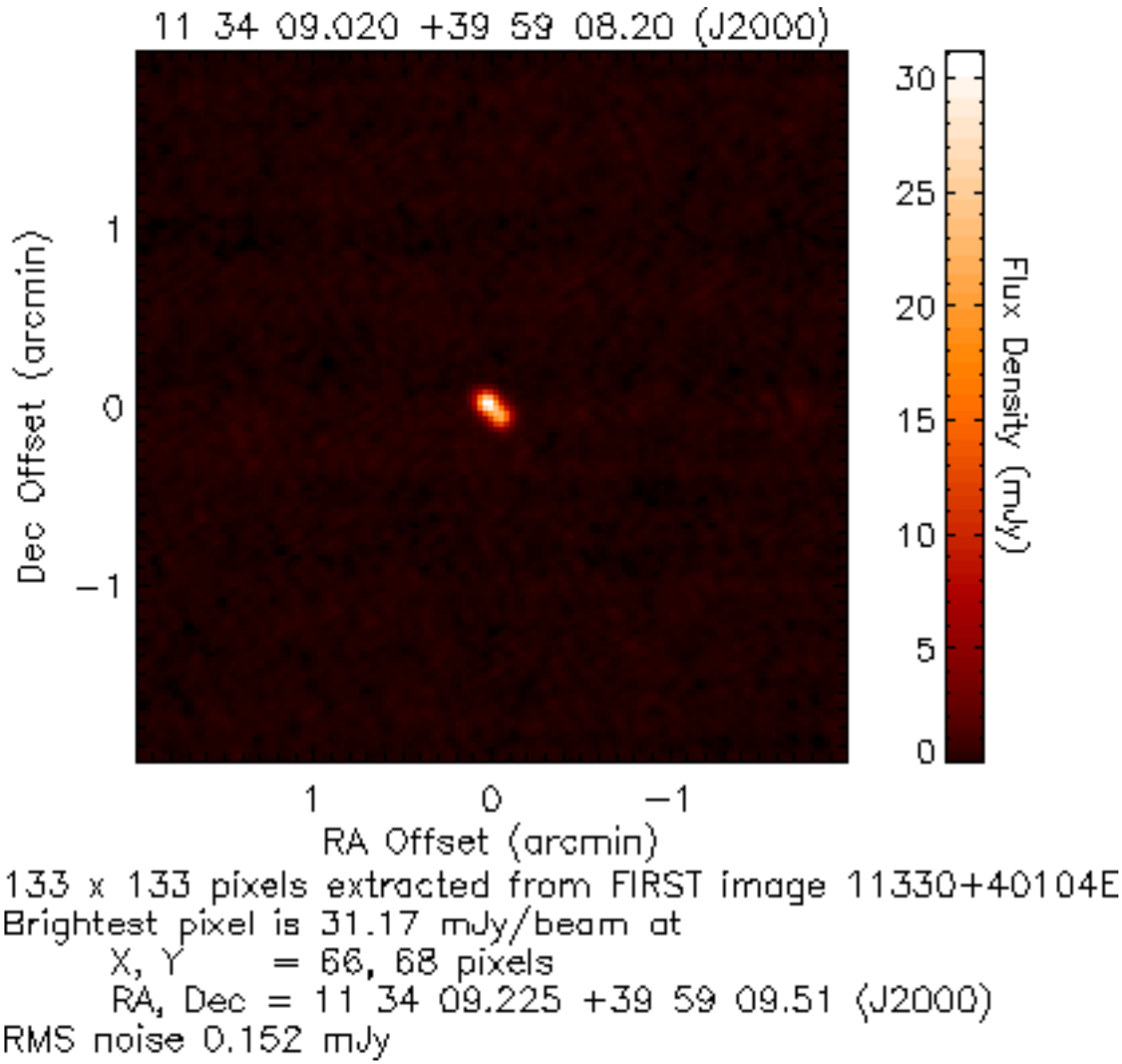

Fig. 12.— FIRST Survey image of a strong type II quasar candidate now identified as radio-loud. The object is double-lobed so the observed radio flux is from relativistic jets. Information on this quasar's radio properties can be found on the first line of table **??**

two coadded spectra also exhibit an emission line between C IV and C III in addition to He II. The coadded spectra tend to be very noisy at the extreme ends because there are fewer spectra covering this range.

4. Conclusion

We are only beginning to develop a robust sample of high redshift radio-quiet type II quasars. The SDSS has allowed us to discover many more candidates at high redshift. In this paper we presented 207 SDSS-selected type II quasar candidates of which we believe 87 are very strong candidates displaying all of the features we would expect of type II quasars– narrow permitted emission lines and extremely low continuum. Eight of these candidates had FIRST survey matches confirming their classification as quasars but because they are radio-loud they do not fit into our sample of interest.

In section 2 the selection criteria were described. Candidates were first selected by σ width < 1500km/s (the criteria of Yesuf (2008)). We then removed objects with any *zwarning* or line area < 0 as they are more likely to be noise (though future studies might examine spectra with a *zwarning* flag set). Finally, objects were visually inspected and classified as either candidate NLS1s or type II quasars. Of the 930 candidates inspected 207 were found to be type II quasar candidates. Of this sample, all but one fit the line width criteria set by Zakamska et al. (2003) (FWHM < 2000 km/s). In addition, by matching to the FIRST survey we discovered that eight of our objects were instead radio-loud quasars.

In section 3 we constructed several composite spectra from various parts of our sample. We noted that these spectra all contained a broad component in the emission line of Lyα and a composite of our less certain candidates also contained a broad component in C IV. These broad components do not rule out type II classification but do require further investigation.

We hope to conduct follow-up observations in the IR and using polarimetry to confirm our classification. A strong ratio of $L_{IR}/L_{optical}$ would confirm obscuration while the existence of polarized light in our sample would help explain broadening at the base of observed emission lines. In the future, HST observations might allow us to observe the host galaxy of any likely type II quasars.

Acknowledgements:

The author would like to acknowledge the invaluable contribution of Dr. Michael Strauss, Professor of Astrophysics at Princeton University and JP advisor extraordinaire. In addition, she is most grateful to Dr. Nadia Zakamska who was never short of helpful suggestions. Also thank you to Sarah Wellons and Tim Brandt for understanding computers. Finally a big thank you to Margaret, Matt and Mary as well as everyone else in room 29 for the friendship and support.

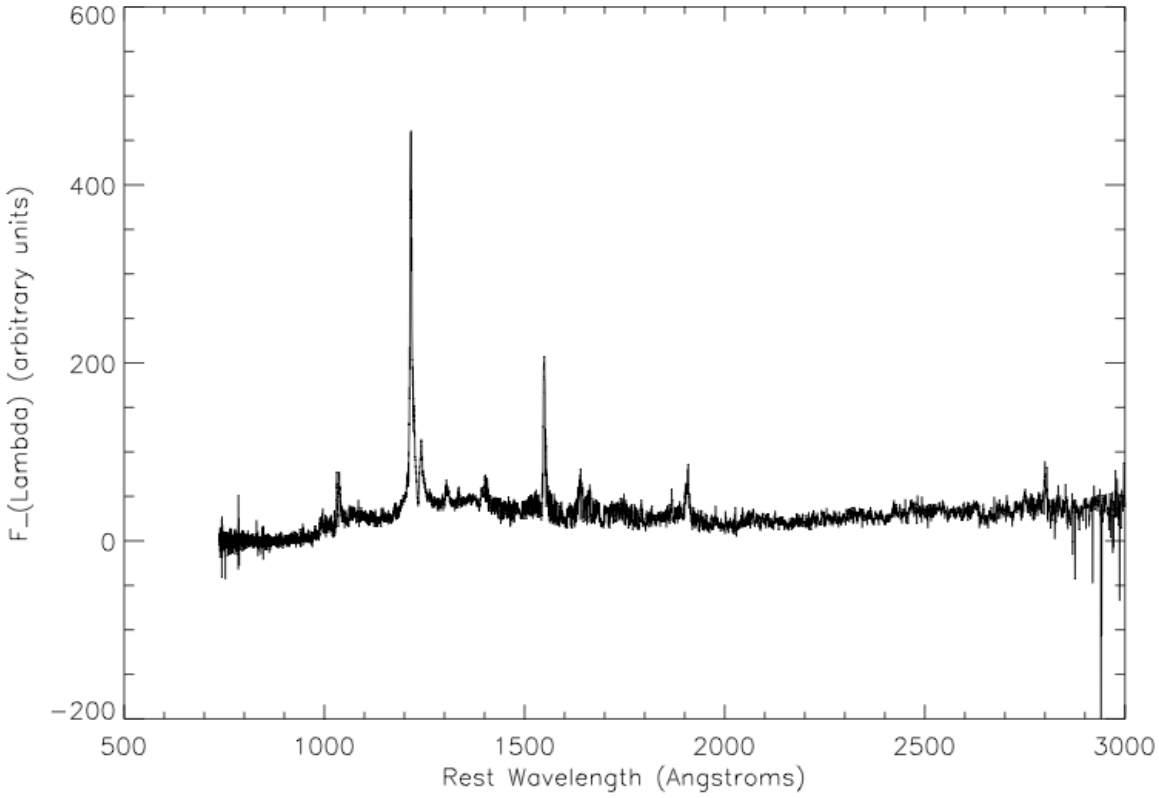

Fig. 13.— Average composite of strong type II quasar candidates. Interestingly, while the CIV line appears very narrow in this coadded spectra, the Lyα emission line does appear to have a bit of a broad base.

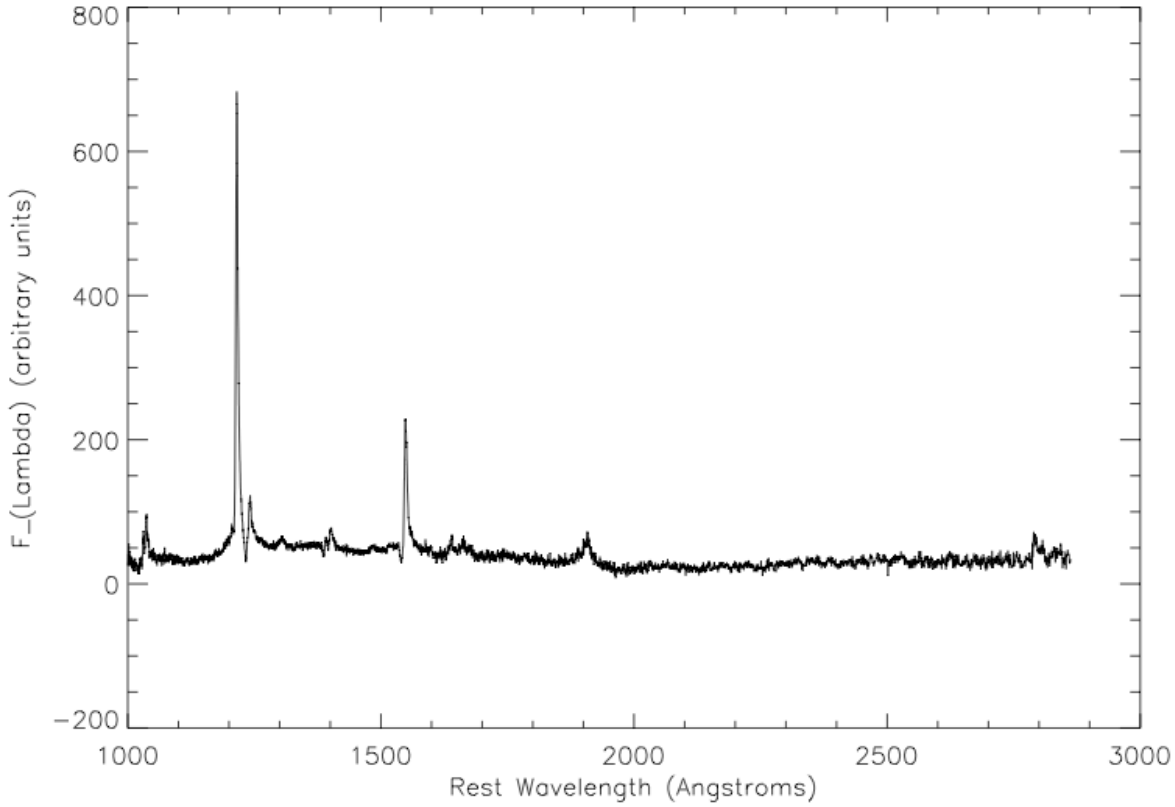

Fig. 14.— Average composite of less clear type II quasar candidates. The Lyα, C IV and C III emission lines all seem to show some broadening though it looks as though this is tempered by absorption on the bluer side of the emission line.

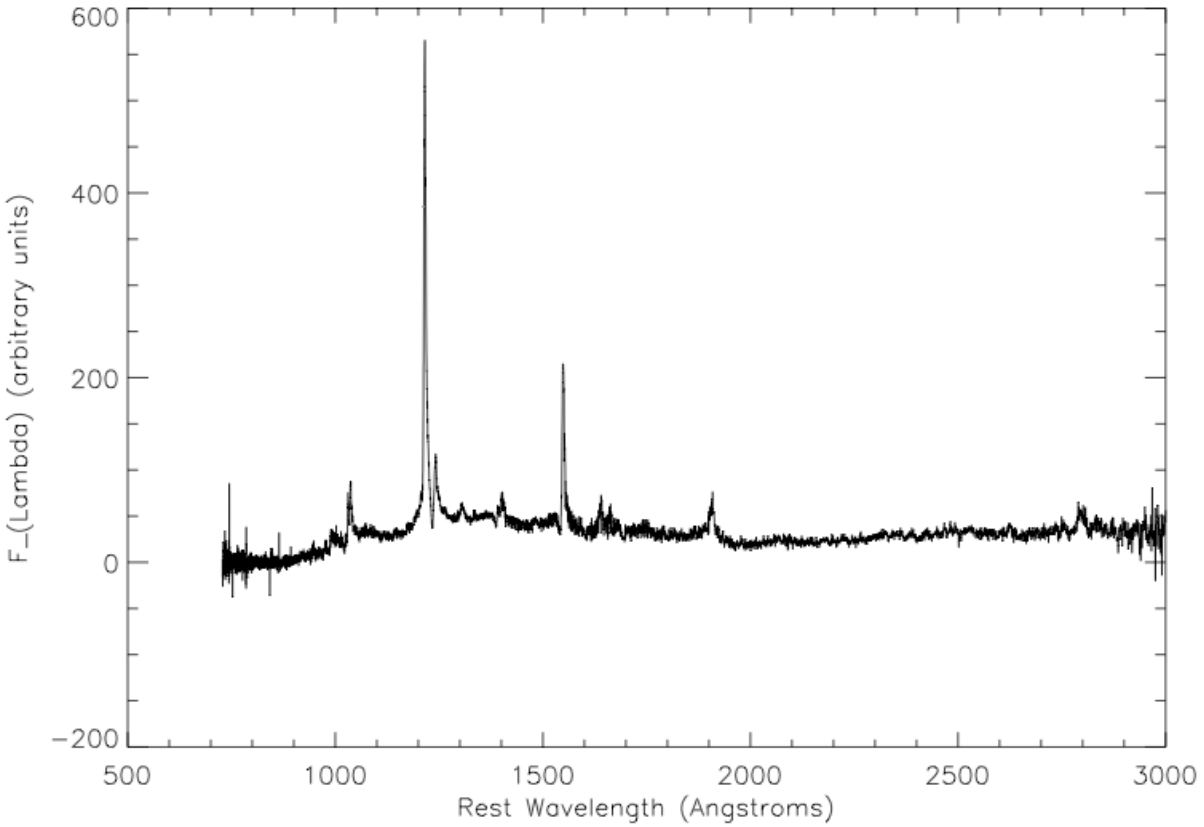

Fig. 15.— Average composite of all potential type II quasar candidates. Some broadening of the Lyα, C IV and C II emission lines can be observed.

Facilities: Sloan Digital Sky Survey

A. Sample Spectra

Below are some examples of spectra observed during this search.

B. Tables of candidate type 2 quasars

Below are the details for the type II quasar candidates identified.

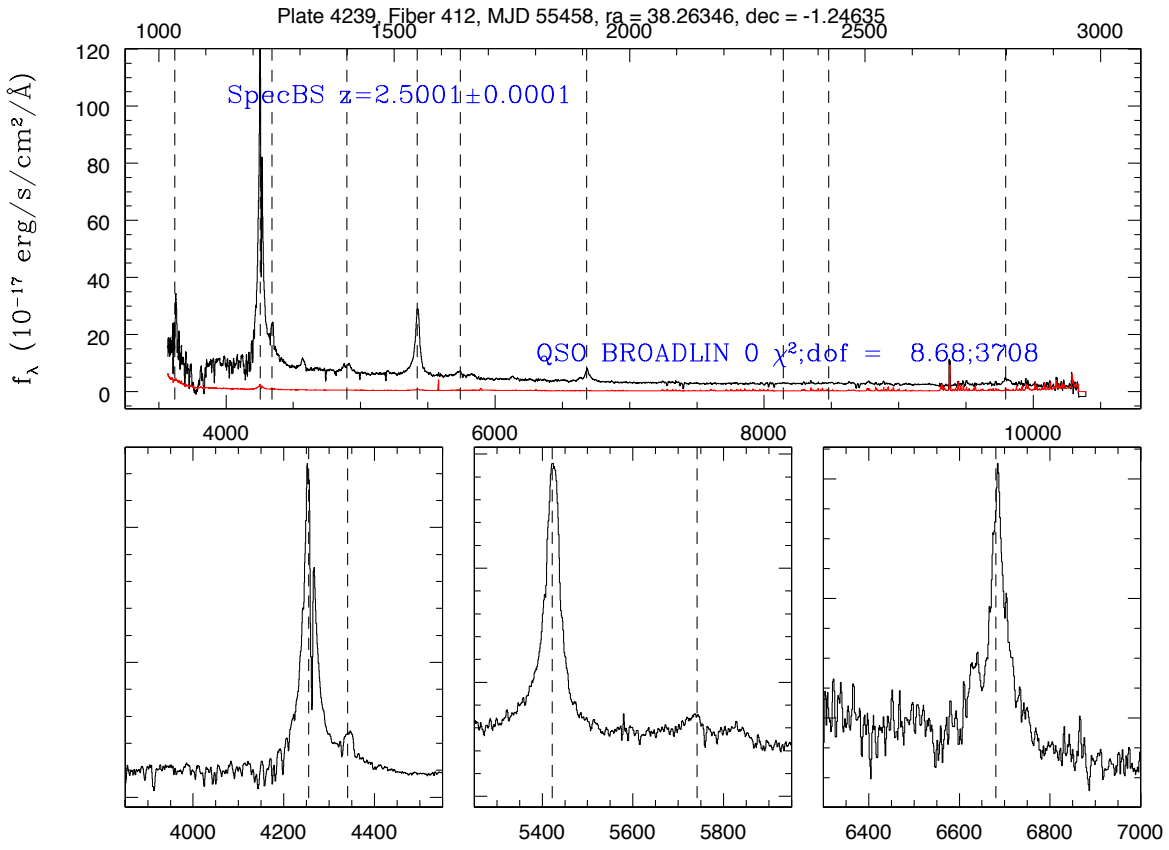

Fig. 16.— Spectrum of a NLS1 identified in our sample of candidates. The top panel shows the entire spectra while the bottom three panels zoom-in on emission lines of interest (Lyα and N V λ 1240 left, C IV λ 1549 and He II λ 1640 center and C III λ 1908 right). Vertical dotted lines on every panel mark emission lines for which data has been collected. The top panel displays rest wavelength along the top and wavelength at the given redshift along the bottom. The red line is a measure of the noise level per pixel. The redshift is given on the top left while the bottom right displays both the object's classification (in our case always "QSO" or quasi-stellar object) and sub-classification if given (in our case "BROADLINE" which means the spectra has an emission line detected at the 10σ level with $\sigma > 200$km/s at the 5σ level). This object was classified as a NLSI because it exhibits emission lines with substantial broadening and a high, blue continuum all of which are characteristics of unobscured objects.

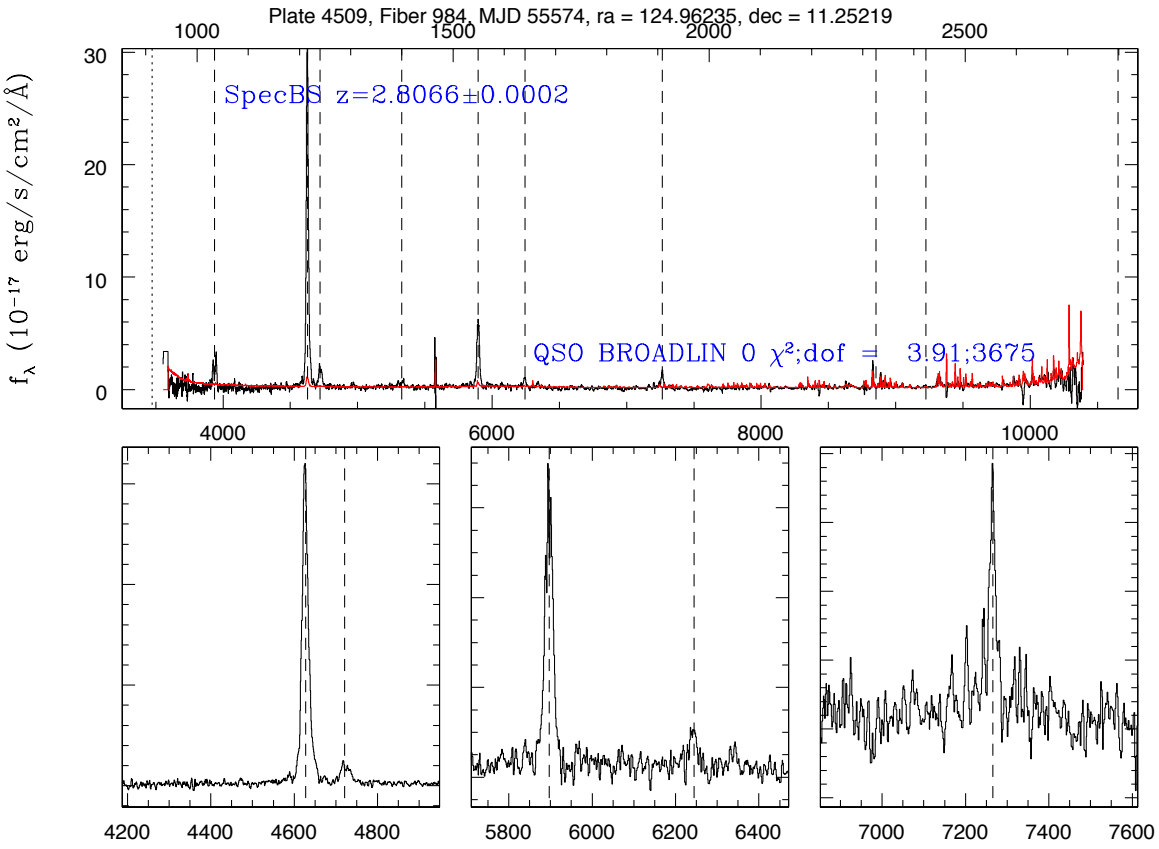

Fig. 17.— Spectrum of a clear type II quasar candidate. This object was identified as a strong type II candidate because of its extremely narrow emission lines and almost nonexistent continuum both of which suggest the central engine of the quasar is obscured.

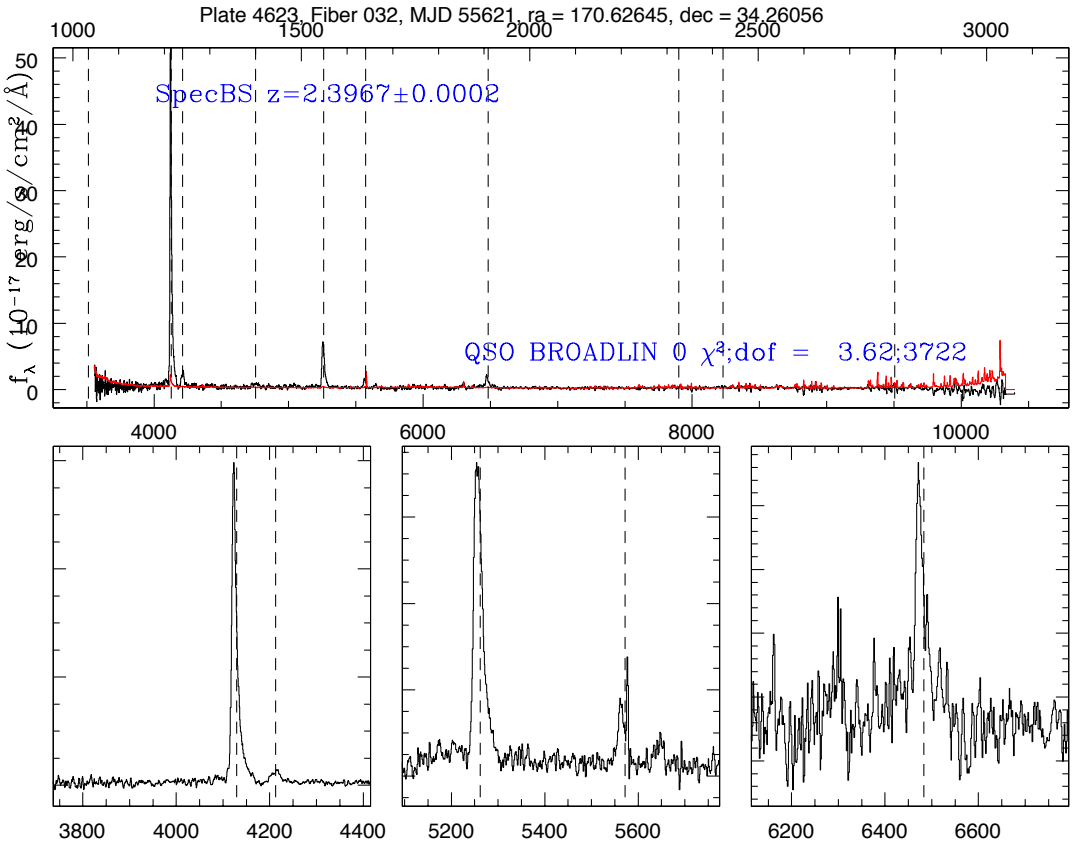

Fig. 18.— Spectrum of a clear type II quasar candidate. This object was identified as a strong type II candidate because of its extremely narrow emission lines and almost nonexistent continuum both of which suggest the central engine of the quasar is obscured. Interestingly, the object does display a tiny amount of broadening to the right of emission lines.

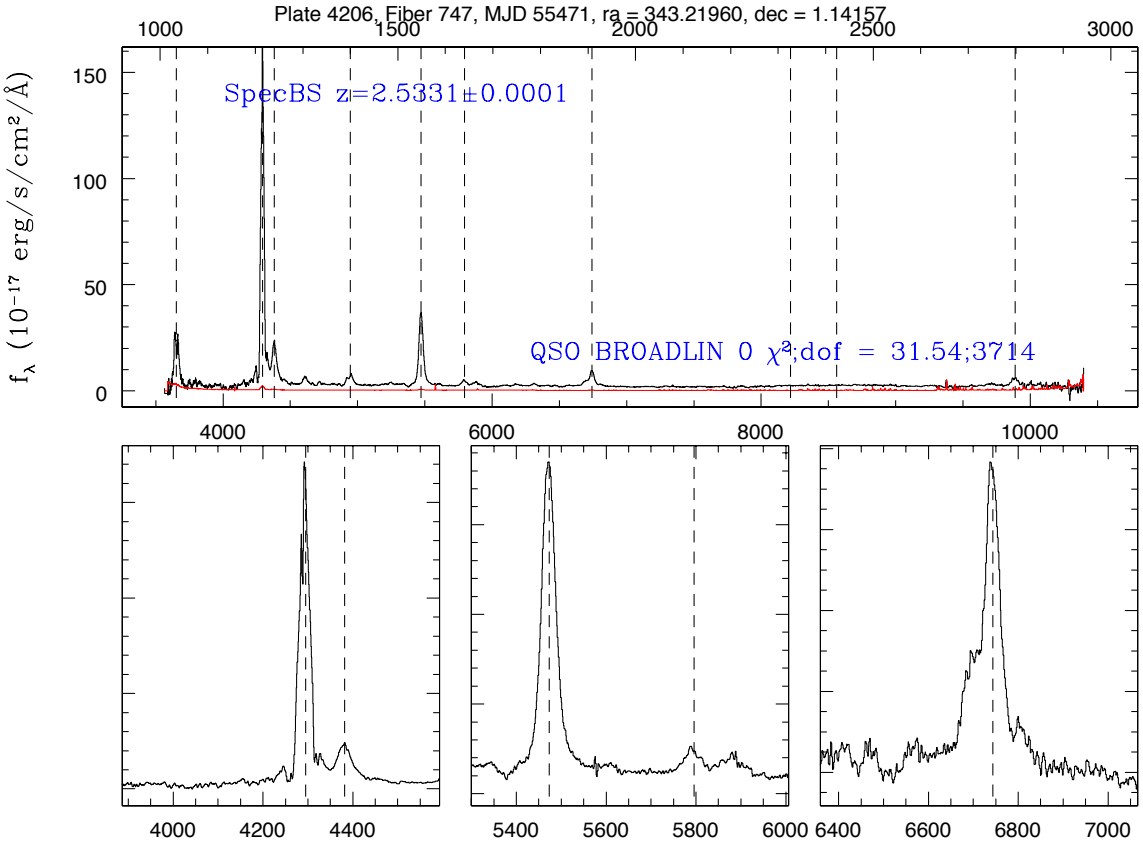

Fig. 19.— Spectrum of a clear type II quasar candidate with an anomaly in the CIII feature. This object was identified as a strong type II candidate because of its extremely narrow emission lines and almost nonexistent continuum both of which suggest the central engine of the quasar is obscured. Interestingly, while both the Lyα and C IV lines exhibit the narrowness expected of a type II obscured quasar the C III line appears much broader. One hypothesis is that there is an emission line of another element transition not being searched for by SDSS that is appearing strongly in this candidate and so broadening the line.

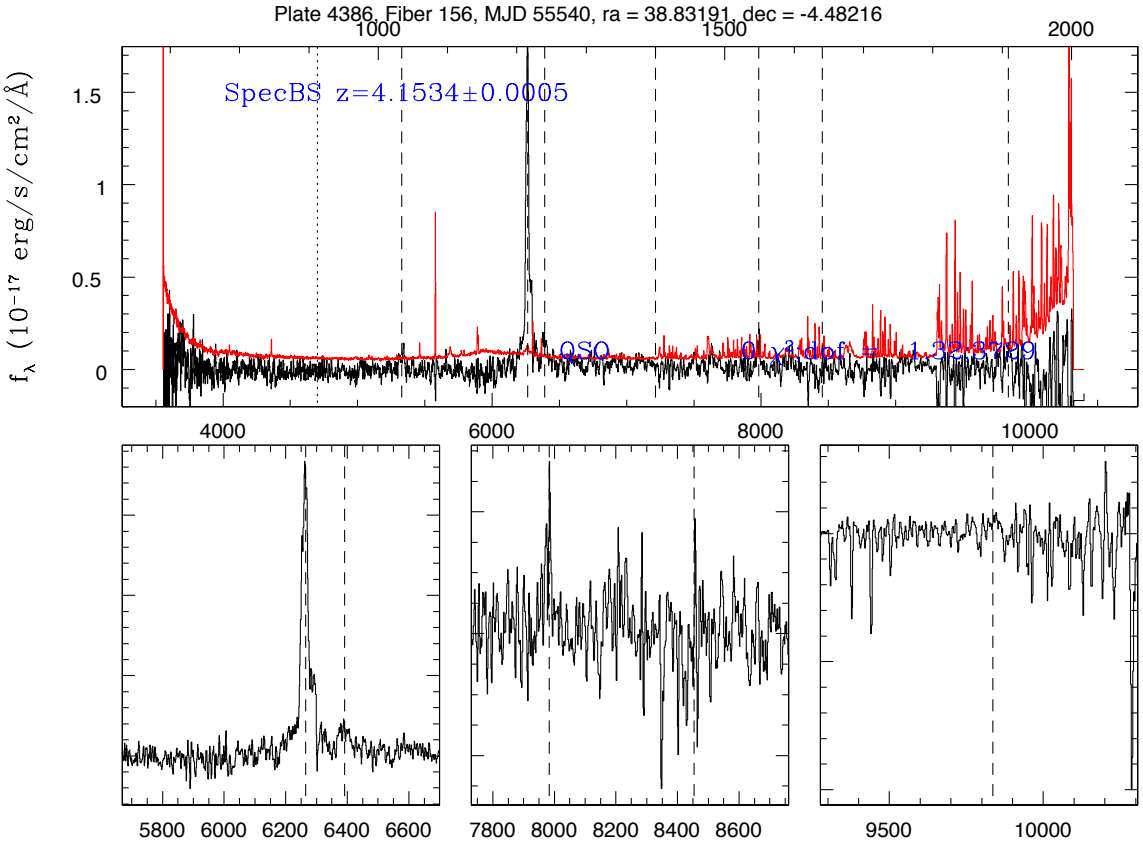

Fig. 20.— Spectrum of the highest redshift clear type II quasar candidate. This object was identified as a strong type II candidate because of its extremely narrow emission lines and almost nonexistent continuum both of which suggest the central engine of the quasar is obscured.

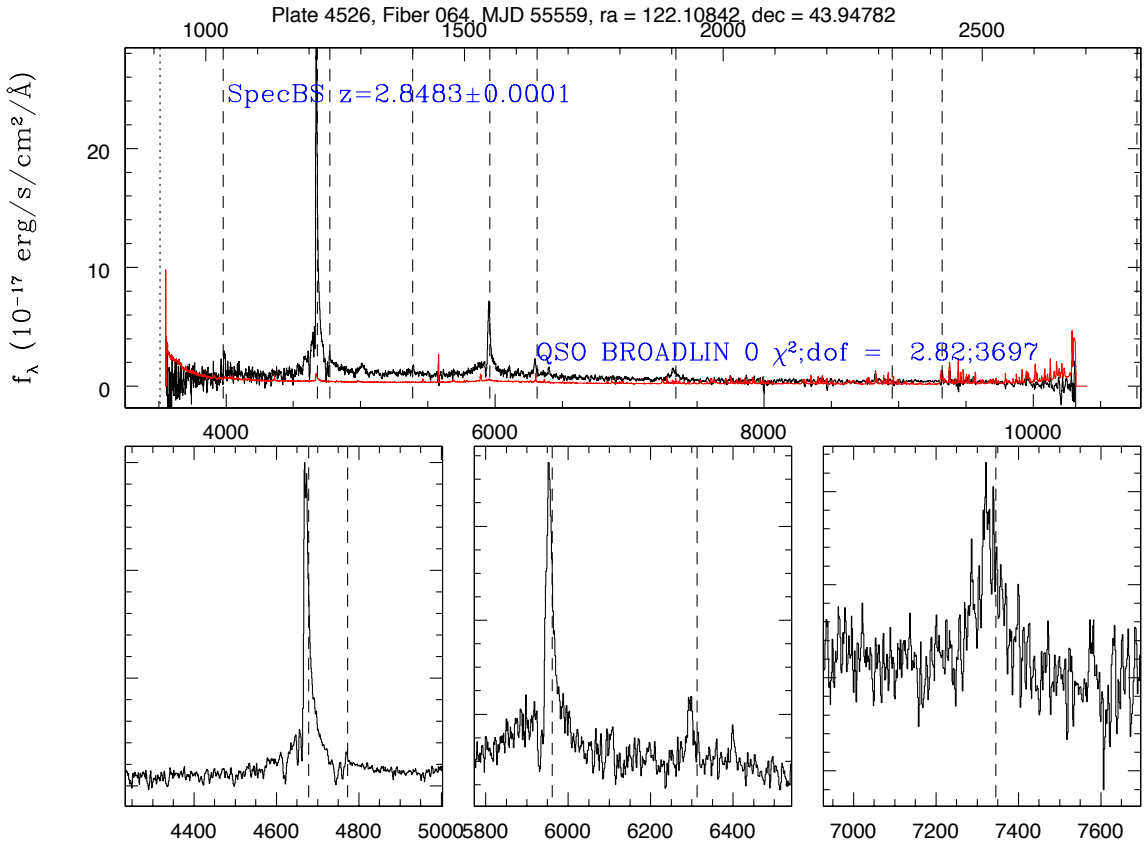

Fig. 21.— Spectrum of a candidate with very narrow emission lines but a broad base component. Even with a broad base it is possible that this object is still a type II quasar. The broad component might be light from the central engine that has scattered off dust clouds near the quasar and been reflected along the line of sight instead of broad emission lines from the central region of the AGN.

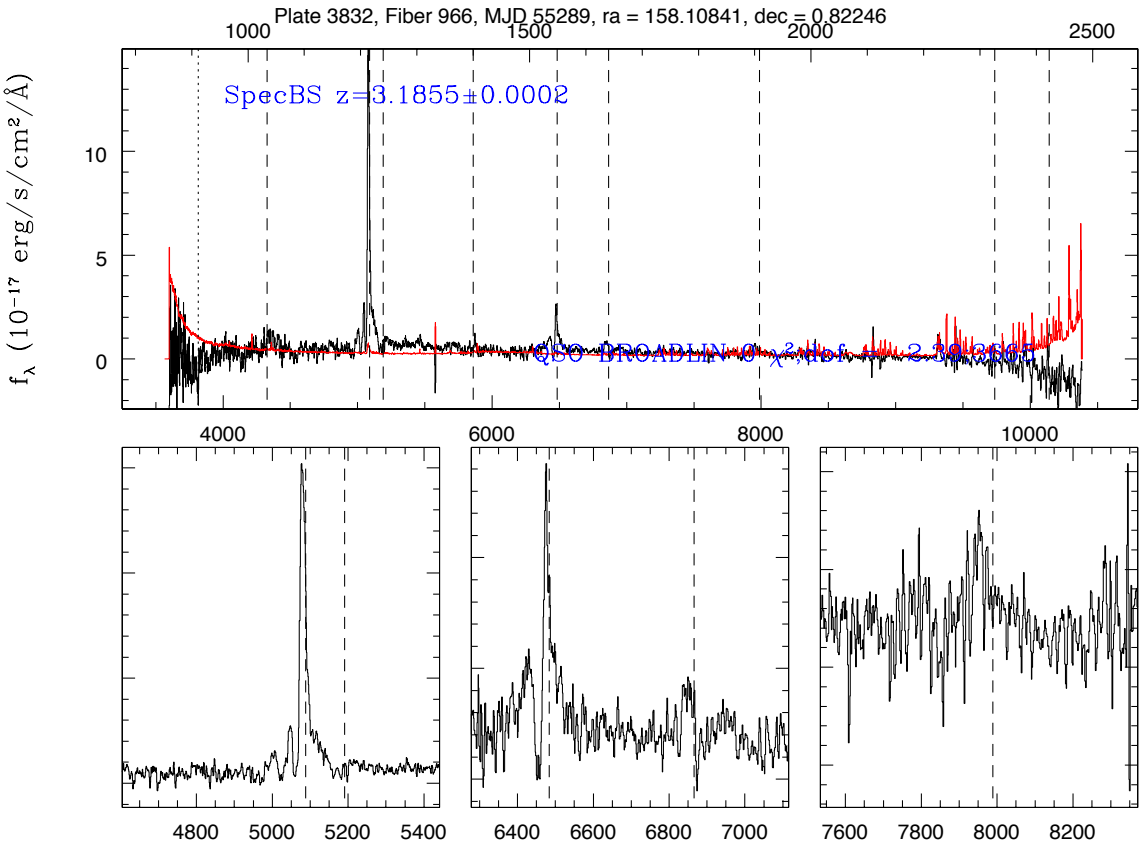

Fig. 22.— Spectrum of a candidate with very narrow emission lines but a broad base component absorbed on one side. The absorption feature is probably the result of dust in the surrounding galaxy. The broad component might be light from the central engine that has scattered off dust clouds near the quasar and been reflected along the line of sight instead of broad emission lines from the central region of the AGN.

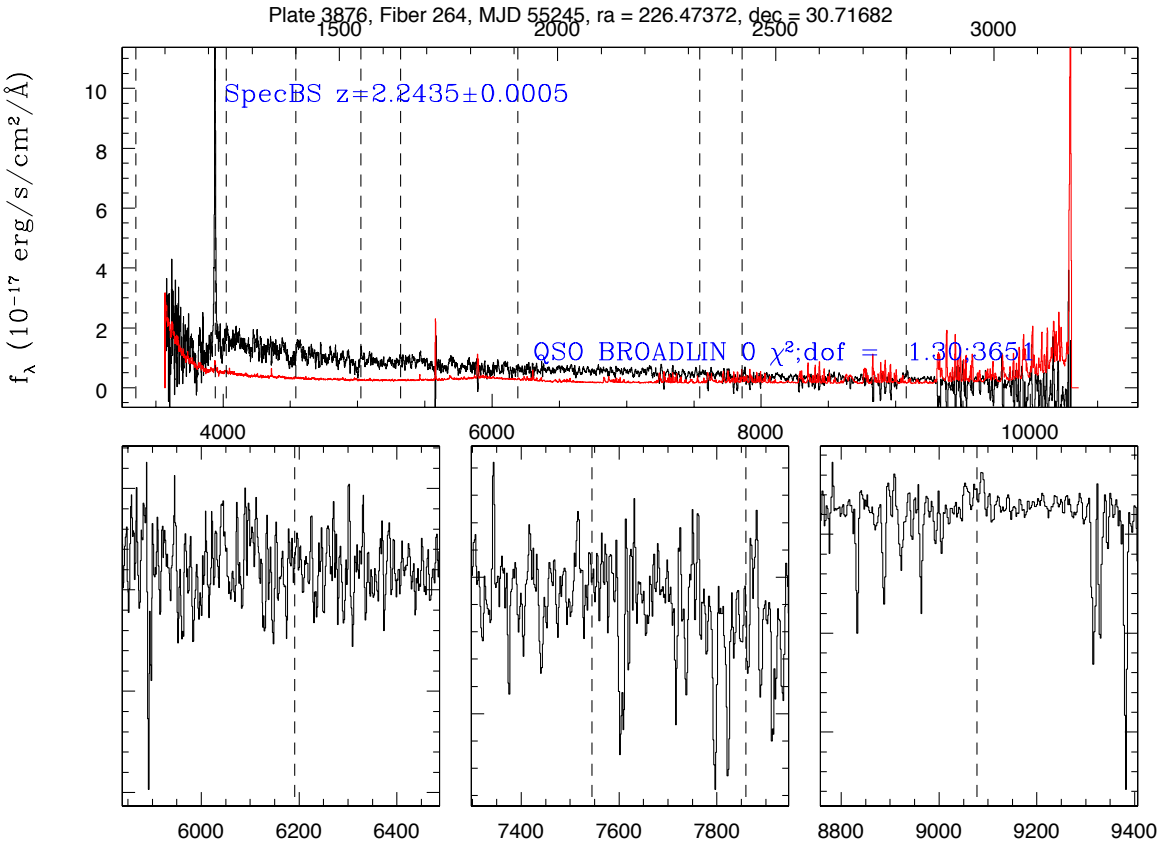

Fig. 23.— Spectrum of a candidate with very narrow lines but a blue continuum that indicates it is not an obscured quasar.

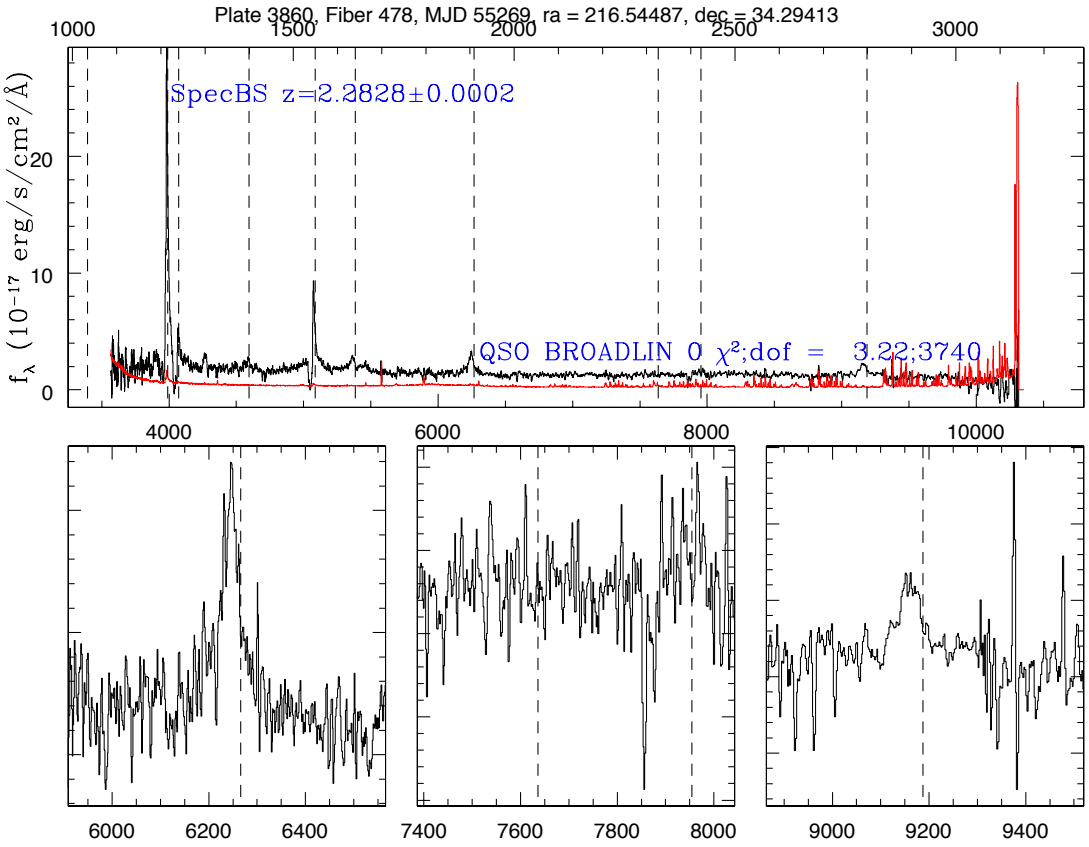

Fig. 24.— Spectrum of a candidate with very narrow lines but a strong continuum that indicates it is not an obscured quasar.

Table 1. Table of our strong Type II quasar candidates

SDSS Name	Plate	Fiber	RA (deg)	DEC (deg)	z	C IV σ (km/s)	dσ
024509.57-003919.2	3651	222	41.2899	-0.655338	2.8485	63.6704	24.09
011954.69-004123.0	4227	2	19.9779	-0.689729	2.80389	195.079	24.13
151747.00+005550.7	4014	908	229.446	0.930763	2.65271	488.903	10.89
081257.15+181916.8	4493	792	123.238	18.3213	2.3813	336.245	19.95
003519.74-005238.7	3587	336	8.83224	-0.87742	3.12856	369.218	41.86
102317.94-010303.0	3831	96	155.825	-1.05084	1.71176	432.001	20.72
083123.63+395822.1	3761	980	127.848	39.9728	3.45565	444.763	27.75
095334.96+003724.4	3828	602	148.396	0.623443	2.6021	631.29	6.00
213733.89+080442.3	4088	812	324.391	8.07842	2.64247	337.275	11.63
103226.02+004920.8	3832	966	158.108	0.822458	3.18035	344.134	21.78
023217.83-081230.3	4389	699	38.0743	-8.20842	3.20391	421.911	17.50
073637.54+225917.4	4470	486	114.156	22.9882	2.26833	489.458	13.63
144227.31-004725.0	4022	362	220.614	-0.79029	2.91578	419.037	39.08
134143.22+365405.5	3986	902	205.43	36.9015	4.11818	452.577	41.48
160103.86+195436.2	3930	146	240.266	19.9101	2.4454	517.722	12.69
081452.05+180602.9	4493	878	123.717	18.1008	3.30295	479.466	19.37
141513.05+023034.5	4030	738	213.804	2.50959	2.77881	642.113	14.77
105616.01+392002.3	4625	452	164.067	39.334	2.17269	523.771	27.68
124530.16+014627.2	4756	382	191.376	1.77423	2.45794	537.261	28.51
103249.55+373649.0	4559	188	158.206	37.6136	2.34863	599.351	13.60
015746.25+102459.2	4530	969	29.4427	10.4164	2.60762	523.143	46.55
023359.27+005925.8	4239	666	38.497	0.990508	2.5425	505.518	68.88
073922.39+345043.6	4440	880	114.843	34.8454	2.13839	656.245	11.62
082726.76+214557.1	4478	308	126.861	21.7659	2.62555	567.99	20.32
155413.91+165128.2	3926	156	238.558	16.8578	2.49474	599.026	16.52
002059.05+030633.4	4300	716	5.24604	3.10928	2.19073	540.201	43.74
073851.85+422010.9	3669	410	114.716	42.3364	2.18807	636.738	14.51
094728.10+363033.2	4573	614	146.867	36.5092	3.05425	677.269	19.77
163758.25+210125.3	4183	610	249.493	21.0237	3.26105	609.228	26.96
082507.42+113117.1	4508	198	126.281	11.5214	2.43142	650.677	20.11
023519.66-042855.8	4386	156	38.8319	-4.48216	4.14894	540.474	109.31
081417.20+140532.5	4504	592	123.572	14.0924	2.2105	814.884	17.17
155725.27+260252.8	3940	680	239.355	26.048	2.82289	629.303	34.38
011509.74+025414.4	4312	129	18.7906	2.904	2.23672	685.9	17.99
225252.70+010829.6	4206	747	343.22	1.14157	2.5313	893.057	3.36
094507.88+353438.0	4575	48	146.283	35.5772	2.99871	52.6664	17.25
160900.02+190534.8	3924	137	242.25	19.093	2.53827	515.845	4.22
150553.69+304300.5	3876	264	226.474	30.7168	2.24445	225.264	51.85

Table 1—Continued

SDSS Name	Plate	Fiber	RA (deg)	DEC (deg)	z	C IV σ (km/s)	dσ
214409.92+090141.2	4093	68	326.041	9.02812	3.81926	230.008	55.17
023828.29-001539.4	3650	354	39.6179	-0.260941	2.81059	276.541	86.31
095819.35+013530.5	4737	336	149.581	1.59181	3.05507	391.544	16.45
115947.86+351418.6	4610	518	179.949	35.2385	2.46792	332.652	29.68
022051.68-012403.3	4345	750	35.2153	-1.40093	2.59778	629.182	11.07
081950.96+111507.9	4509	984	124.962	11.2522	2.80553	460.831	11.08
080826.02+435652.2	4526	64	122.108	43.9478	2.84322	446.416	17.00
084949.57+044330.9	3811	826	132.457	4.72526	3.09045	436.071	13.66
023337.89+002303.7	3745	604	38.4079	0.384358	2.82856	347.226	41.29
215341.33+041132.7	4096	406	328.422	4.19241	2.40941	493.521	10.59
113409.02+395908.2	4655	184	173.538	39.9856	1.54972	454.465	10.91
121350.37+040629.5	4749	226	183.46	4.10819	3.05519	359.742	32.30
134240.84-004540.6	4043	340	205.67	-0.76128	2.3034	351.77	47.34
080826.02+435652.2	3685	72	122.108	43.9478	2.84295	439.952	27.76
075707.16+201513.0	4482	300	119.28	20.2536	3.13898	379.966	23.25
220126.11+001231.5	4199	540	330.359	0.20876	2.63098	441.176	13.57
015700.14+073116.0	4531	260	29.2506	7.52111	3.04591	445.094	12.72
112230.35+341538.0	4623	32	170.626	34.2606	2.39311	507.001	10.43
013327.23+001959.6	4230	684	23.3635	0.333224	2.71645	495.342	9.01
222946.61+005540.5	4203	612	337.444	0.927919	2.36308	514.576	9.34
001738.55-011838.7	4366	744	4.41064	-1.31075	3.22026	383.709	31.50
113351.03+400851.1	4655	232	173.463	40.1475	3.00059	441.094	18.62
114753.29+313152.4	4614	244	176.972	31.5312	2.46341	416.165	21.72
020245.82+000848.4	4234	858	30.6909	0.146777	2.21308	423.409	16.11
220126.11+001231.5	3549	616	330.359	0.20876	2.63166	472.527	19.75
091301.34+034207.6	3820	230	138.256	3.7021	3.00405	450.008	28.18
105344.18+395402.3	4629	886	163.434	39.9006	3.22102	491.342	17.96
100133.86+415107.9	4566	626	150.391	41.8522	2.35865	539.787	13.22
133059.33+014610.3	4045	232	202.747	1.76954	2.33799	458.644	23.96
011506.65-015307.0	4353	616	18.7777	-1.88528	2.32545	571.126	10.85
151246.27+022129.5	4013	896	228.193	2.3582	2.65055	458.36	32.35
161353.27+201526.5	4057	488	243.472	20.2574	2.96496	473.324	36.58
225607.62+052520.2	4293	784	344.032	5.42228	3.14892	510.907	15.88
091025.51+042944.4	3820	655	137.606	4.49566	3.77297	561.661	16.19
221601.20+032056.1	4319	452	334.005	3.34891	2.40938	496.474	27.75
151815.55+273618.0	3851	350	229.565	27.605	3.32975	581.015	10.73
223348.09+024932.9	4291	346	338.45	2.82579	2.58386	572.009	18.46
074539.44+380029.0	3670	339	116.414	38.0081	3.19798	493.303	50.74

Table 1—Continued

SDSS Name	Plate	Fiber	RA (deg)	DEC (deg)	z	C IV σ (km/s)	dσ
143305.81-025536.8	4029	166	218.274	-2.92689	3.19624	546.852	25.89
022447.84+032452.0	4265	752	36.1993	3.41444	2.52611	512.537	33.81
112343.18-010315.7	3774	835	170.93	-1.05435	2.16614	511.124	38.20
124302.62+421245.3	4702	926	190.761	42.2126	2.40842	573.386	20.29
144441.05-001343.4	4022	278	221.171	-0.228733	2.54415	591.768	14.27
225558.19-001802.4	4206	84	343.992	-0.300673	2.58204	538.107	29.38
013747.84+000612.7	4231	563	24.4493	0.103531	2.81579	621.777	23.36
015458.32+015720.2	4273	7	28.743	1.95561	2.88662	534.752	64.41
090612.64+030900.4	3819	644	136.553	3.1501	2.49979	617.436	19.93
230146.23-010348.9	3564	402	345.443	-1.06358	3.08476	532.645	112.73
001008.02+000317.5	4217	116	2.53341	0.0548549	2.29114	697.139	10.89

Table 2. Table of our potential Type II quasar candidates

SDSS Name	Plate	Fiber	RA (deg)	DEC (deg)	z	C IV σ (km/s)	dσ
120116.06+005709.6	3844	598	180.317	0.952673	2.43773	474.997	18.38
020214.98+044204.9	4268	686	30.5624	4.70136	2.47292	487.807	17.75
155906.48+243929.8	3934	524	239.777	24.6583	2.76821	551.287	15.08
073018.99+411947.3	3656	10	112.579	41.3298	3.10666	547.094	33.92
100247.14+002053.0	3829	682	150.696	0.348057	2.21805	533.65	24.79
213135.44+082445.8	4088	556	322.898	8.41272	3.73459	580.067	32.91
081812.72+223755.3	4479	768	124.553	22.632	2.45283	568.845	36.05
114042.05+374337.8	4653	572	175.175	37.7272	2.51197	550.099	17.58
130907.84+020547.6	4007	616	197.283	2.09655	2.22662	680.165	14.02
123835.84-030007.0	3778	124	189.649	-3.00194	2.99911	553.148	6.73
142610.77+341738.8	3860	478	216.545	34.2941	2.27718	429.564	11.16
234612.64+005154.0	4280	204	356.553	0.865009	2.30905	468.982	13.02
213401.62+041225.8	4084	93	323.507	4.20717	2.3285	418.765	18.51
151158.88+275203.5	3872	928	227.995	27.8676	2.69668	436.818	13.45
114856.13+012731.6	4729	180	177.234	1.45878	2.32725	442.209	19.62
112609.79+344821.7	4619	658	171.541	34.806	2.46026	397.478	146.61
094308.14+380923.0	4572	412	145.784	38.1564	3.11258	408.77	46.99
095534.23+011801.9	3828	708	148.893	1.30053	3.21761	432.491	32.74
144437.72-013625.8	4023	502	221.157	-1.60716	2.25253	708.224	10.52
002441.00+004557.8	4220	598	6.17081	0.766044	2.23527	629.658	10.25
020249.27-000138.9	3609	360	30.7053	-0.0274837	2.36482	441.674	32.02
163015.06+160118.3	4056	888	247.563	16.0217	2.61814	434.955	45.98
143714.02-024707.4	4026	356	219.308	-2.78538	2.95966	467.301	34.60
080818.28+135921.8	4499	324	122.076	13.9894	3.11937	474.142	31.72
224739.27-014817.0	4363	924	341.914	-1.80473	2.46815	450.064	34.22
025821.48-015211.3	4341	968	44.5895	-1.86981	2.37306	437.412	71.55
082625.94+312600.8	4446	110	126.608	31.4336	2.40087	497.646	19.01
020245.82+000848.4	3609	698	30.6909	0.146777	2.21366	507.752	21.02
145932.09+301953.9	3875	106	224.884	30.3316	2.55825	576.457	13.68
131914.83+041730.4	4761	646	199.812	4.29179	2.24472	562.068	25.57
134018.78-021725.0	4047	872	205.078	-2.29027	2.34088	495.711	20.14
081328.31+500551.6	4527	4	123.368	50.0977	2.4166	478.065	31.98
005018.67+050132.6	4305	907	12.5778	5.02571	2.93831	489.767	32.11
022119.01+000618.4	4237	736	35.3292	0.105116	2.85731	491.467	26.69
083402.35+325106.6	4445	728	128.51	32.8518	2.57276	496.595	30.50
003519.74-005238.7	4221	176	8.83224	-0.87742	3.12904	475.372	37.01
133507.39+001446.0	4046	764	203.781	0.246123	2.51015	510.354	26.13
093018.43+363933.9	4576	808	142.577	36.6594	2.27221	509.428	39.22

Table 2—Continued

SDSS Name	Plate	Fiber	RA (deg)	DEC (deg)	z	C IV σ (km/s)	dσ
230856.81+001656.5	4208	898	347.237	0.282356	3.82388	486.343	45.68
161816.89+225538.3	3928	977	244.57	22.9273	3.60425	536.444	15.15
123212.97+392619.0	3970	482	188.054	39.4386	2.4264	588.492	19.82
113528.57+340333.3	4616	654	173.869	34.0593	2.54403	539.547	29.30
210919.92+085913.3	4079	742	317.333	8.98703	2.27166	689.139	12.54
131553.17+005152.2	4004	758	198.972	0.864509	2.24806	571.988	16.81
024659.29-001709.1	4240	36	41.747	-0.285864	2.44577	531.601	25.23
010554.40+011326.9	4226	636	16.4767	1.22413	3.06	550.426	29.81
004728.77+004020.3	3589	916	11.8699	0.672305	3.06318	541.786	40.60
154335.34+171628.6	3932	308	235.897	17.2746	2.34368	568.808	23.43
004024.39+004504.2	4222	712	10.1016	0.751175	3.76884	579.131	16.56
154222.88+205752.8	3937	742	235.595	20.9647	2.95548	521.593	56.02
160747.25+162123.6	4072	358	241.947	16.3566	4.21848	542.8	32.85
211926.12-011442.9	4192	202	319.859	-1.24524	3.11722	539.596	35.37
160042.75+235618.1	3934	476	240.178	23.9384	2.45323	637.811	14.57
145425.19+013421.1	4018	12	223.605	1.57252	2.61572	626.612	19.93
090731.89+001138.0	3818	858	136.883	0.19388	2.28474	585.187	15.36
155530.64+195741.8	3931	862	238.878	19.9616	2.26234	538.05	47.31
131928.97-014814.3	4049	604	199.871	-1.80398	3.03693	720.49	22.55
122119.18+375127.1	3965	522	185.33	37.8575	2.36709	593.529	23.31
014516.90+045227.8	4272	758	26.3204	4.87438	3.27465	646.549	15.73
113812.30+350559.7	4615	60	174.551	35.0999	3.17432	553.968	61.51
143904.06-030257.9	4026	246	219.767	-3.04942	2.5068	632.663	20.77
080754.44+363117.3	3804	427	121.977	36.5215	2.57356	554.305	47.61
081452.05+180602.9	4486	328	123.717	18.1008	3.30388	590.215	26.32
093323.19-012307.1	3767	692	143.347	-1.38531	3.24049	583.331	24.06
212816.06+001520.6	4193	898	322.067	0.255734	2.43606	586.817	21.77
141659.81+343513.2	3863	666	214.249	34.587	2.73737	572.914	40.18
012807.86-001441.2	4229	225	22.0327	-0.244789	2.64784	555.049	45.66
010046.17-005855.3	4225	299	15.1924	-0.982028	3.34928	707.01	13.94
095739.64+385949.6	4570	802	149.415	38.9971	2.75267	604.058	34.43
074850.25+353345.1	3791	310	117.209	35.5625	2.73156	657.678	27.07
131022.41+381640.7	3978	892	197.593	38.278	3.13359	618.126	28.50
153747.30+270549.3	3952	456	234.447	27.097	2.64112	615.427	27.69
025339.00+042154.5	4256	726	43.4125	4.36514	2.84887	624.499	24.62
132316.69+342855.4	3982	399	200.82	34.4821	2.36181	594.516	34.66
023455.23-075453.3	4389	844	38.7301	-7.9148	2.33543	583.482	24.89
115715.88-003044.0	3843	182	179.316	-0.512214	3.07802	583.34	51.45

Table 2—Continued

SDSS Name	Plate	Fiber	RA (deg)	DEC (deg)	z	C IV σ (km/s)	dσ
082556.75+403930.0	3808	377	126.486	40.6583	2.69501	651.689	22.45
101209.32+354417.6	4568	394	153.039	35.7382	2.59237	605.373	40.44
083324.27+215018.2	4478	26	128.351	21.8384	2.77237	633.1	24.63
232503.75+004034.6	4211	646	351.266	0.676283	2.45704	599.607	50.51
114429.16+342343.7	4646	302	176.121	34.3955	3.04019	647.307	30.79
211926.12-011442.9	3538	122	319.859	-1.24524	3.11613	630.749	84.13
105505.45-000820.5	3835	34	163.773	-0.139041	3.70622	685.462	29.93
094431.36+402127.1	4571	152	146.131	40.3575	2.46847	324.392	23.75
155200.53+175722.7	3926	754	238.002	17.9563	2.70073	415.136	13.40
020643.64+010403.3	4235	630	31.6818	1.06759	2.6549	497.221	14.98
023337.89+002303.7	4239	652	38.4079	0.384358	2.82939	391.972	42.31
212055.56+065244.7	4081	636	320.232	6.87908	2.59705	477.004	16.49
001814.72+023258.8	4300	564	4.56134	2.54966	2.90153	384.712	41.36
160925.80+241756.4	3934	38	242.357	24.299	2.71401	588.945	10.55
130242.30+400125.8	3976	902	195.676	40.0238	2.7696	468.889	17.72
104133.36+393325.4	4633	142	160.389	39.5571	2.42817	461.338	11.96
001922.82-004938.2	4219	330	4.84507	-0.827269	3.30622	410.794	28.68
074251.43+224623.2	4470	178	115.714	22.7731	2.98408	411.801	42.20
082530.66+120658.5	4508	844	126.378	12.1162	2.35086	437.492	20.50
212201.19+023844.8	4077	90	320.505	2.64577	2.29757	420.213	44.16
105344.18+395402.3	4625	502	163.434	39.9006	3.22168	509.639	15.22
024520.35-001102.5	4240	114	41.3348	-0.184018	3.1754	493.916	22.71
133417.03+362753.0	3986	552	203.571	36.4647	2.28308	494.808	17.38
001142.42-000845.7	4218	355	2.92675	-0.146017	2.31469	493.116	28.30
014607.15+121120.0	4659	532	26.5298	12.1889	3.13546	557.161	13.86
004600.48+000543.6	4222	1000	11.502	0.0954582	2.45582	517.617	25.31
074725.51+160053.7	4497	885	116.856	16.0149	2.82368	537.048	32.75
091639.37+020022.1	3822	796	139.164	2.00614	2.42748	548.01	17.02
024659.29-001709.1	4241	360	41.747	-0.285864	2.44515	541.016	23.44
082550.58+332543.1	4442	304	126.461	33.4286	2.8676	519.242	39.29
160440.25+213633.5	3929	436	241.168	21.6093	2.34848	534.927	21.06
123449.55+374618.2	3969	648	188.706	37.7717	2.22049	588.923	22.21
012013.40+004311.2	4228	672	20.0559	0.71979	3.01679	568.302	39.68
155715.44+234705.1	3935	702	239.314	23.7847	3.03652	590.299	23.96
150315.27+014046.4	4016	662	225.814	1.67955	2.65376	724.48	16.75
005514.63+002926.1	4224	812	13.811	0.490581	2.78534	607.071	28.82
213843.08-010133.6	4195	298	324.68	-1.02599	2.79641	572.435	38.42
212306.83-005247.8	4192	50	320.778	-0.879937	2.28773	654.525	16.57

C. Table of radio properties of candidate type 2 quasars

D. Interesting Identified Objects Outside the Scope of this Paper

REFERENCES

Bradley W. Carroll, D. A. O. 2007, An Introduction to Modern Astrophysics (Pearson Education Inc.)

Diamond-Stanic, A. M., Fan, X., Brandt, W. N., Shemmer, O., Strauss, M. A., Anderson, S. F., Carilli, C. L., Gibson, R. R., Jiang, L., Kim, J. S., Richards, G. T., Schmidt, G. D., Schneider, D. P., Shen, Y., Smith, P. S., Vestergaard, M., & Young, J. E. 2009, ApJ, 699, 782

Eisenstein, D. J., Weinberg, D. H., Agol, E., Aihara, H., Allende Prieto, C., Anderson, S. F., Arns, J. A., Aubourg, E., Bailey, S., Balbinot, E., & et al. 2011, ArXiv e-prints

Hao, L., Strauss, M. A., Tremonti, C. A., Schlegel, D. J., Heckman, T. M., Kauffmann, G., Blanton, M. R., Fan, X., Gunn, J. E., Hall, P. B., Ivezić, Ž., Knapp, G. R., Krolik, J. H., Lupton, R. H., Richards, G. T., Schneider, D. P., Strateva, I. V., Zakamska, N. L., Brinkmann, J., Brunner, R. J., & Szokoly, G. P. 2005, AJ, 129, 1783

Hogg, D. W. 1999, ArXiv Astrophysics e-prints

Martínez-Sansigre, A., Rawlings, S., Lacy, M., Fadda, D., Jarvis, M. J., Marleau, F. R., Simpson, C., & Willott, C. J. 2006, MNRAS, 370, 1479

Norman, C., Hasinger, G., Giacconi, R., Gilli, R., Kewley, L., Nonino, M., Rosati, P., Szokoly, G., Tozzi, P., Wang, J., Zheng, W., Zirm, A., Bergeron, J., Gilmozzi, R., Grogin, N., Koekemoer, A., & Schreier, E. 2002, ApJ, 571, 218

Reyes, R., Zakamska, N. L., Strauss, M. A., Green, J., Krolik, J. H., Shen, Y., Richards, G. T., Anderson, S. F., & Schneider, D. P. 2008, AJ, 136, 2373

Table 2—Continued

SDSS Name	Plate	Fiber	RA (deg)	DEC (deg)	z	C IV σ (km/s)	dσ
095546.07+380011.3	4570	332	148.942	38.0031	2.47587	605.529	32.51
100210.53+381245.0	4567	494	150.544	38.2125	2.93686	644.799	20.74
115039.48-005852.7	3842	170	177.665	-0.981298	3.02177	605.891	43.85
012510.46+001425.6	4229	612	21.2936	0.240457	2.42717	593.524	26.98
122214.45+374837.9	3965	568	185.56	37.8105	3.15907	635.754	35.17
235441.12+030057.9	4278	836	358.671	3.01607	2.47215	371.906	16.97

Table 3. FIRST radio source matches

Search Distance (arcsec)	RA (2000)	Dec (2000)	Peak Flux (mJy/bm)	Int. Flux (mJy)	RMS (mJy/bm)	Table
0.3	11 34 9.032	+39 59 7.89	31.51	65.76	0.138	1
0.6	11 47 53.301	+31 31 52.99	2.04	1.57	0.278	1
0.1	16 07 47.250	+16 21 23.67	3.44	3.11	0.14	2
0.6	00 24 40.994	+00 45 57.11	48.5	59.35	0.133	2
0.1	10 23 17.935	-01 03 2.93	7.19	7.35	0.215	1
0.2	11 23 43.182	-01 03 15.47	2.09	1.57	0.154	1
1	09 33 23.128	-01 23 7.61	1.13	1.13	0.142	2
0.4	14 44 37.728	-01 36 25.50	5.68	5.33	0.146	2

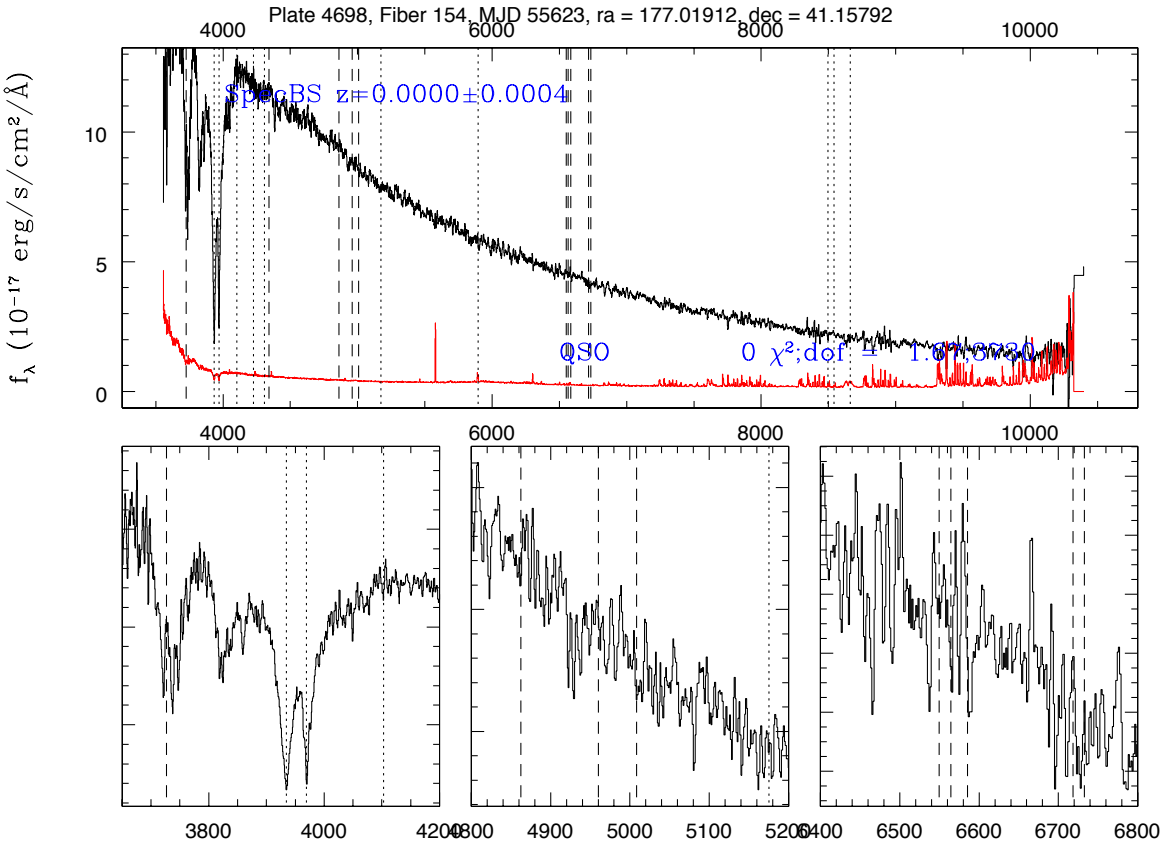

Fig. 25.— Spectrum of a calcium-rich white dwarf. The pipeline incorrectly identified the redshift of this object placing it in our sample. At its proper redshift of zero strong calcium absorption becomes apparent (see bottom left panel).

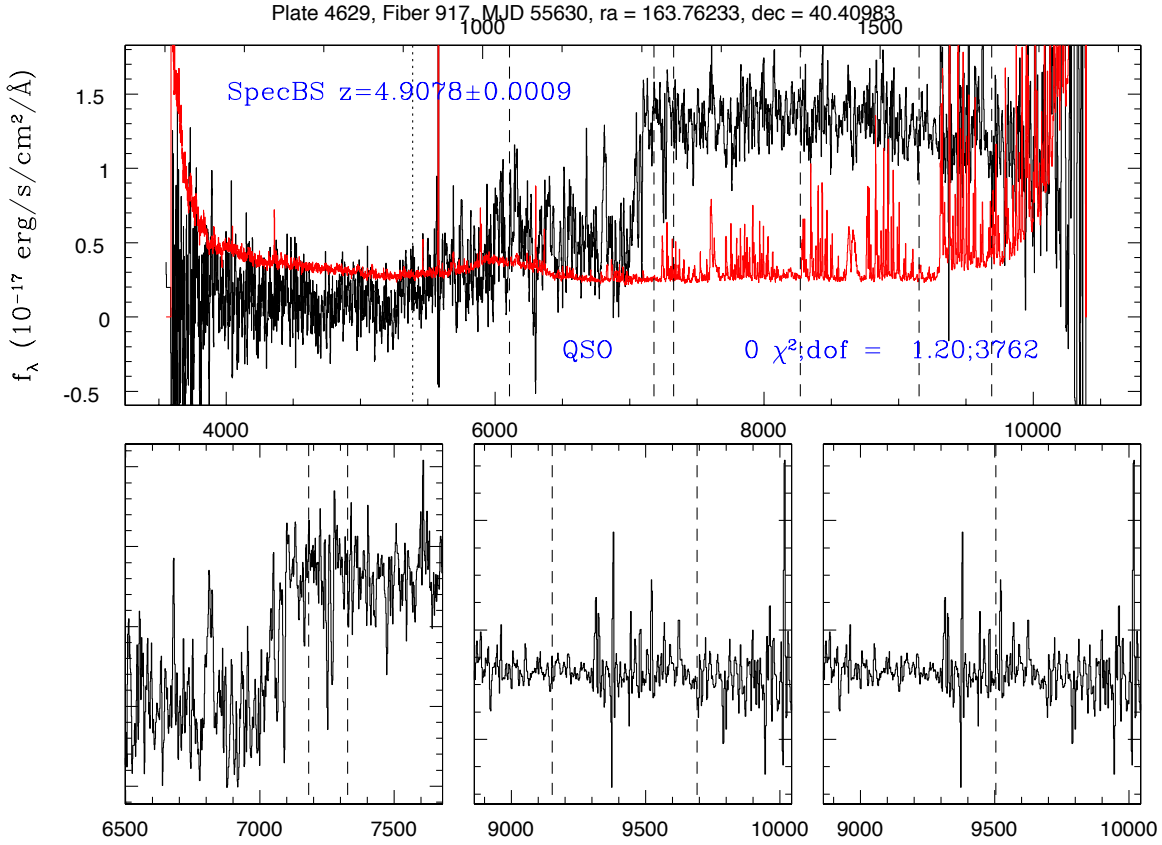

Fig. 26.— Spectrum of a lineless AGN. The Lyα forest is clearly visible but even at longer wavelengths no emission lines are present. See Diamond-Stanic et al. (2009) for other examples from SDSS.

Spergel, D. N., Bean, R., Doré, O., Nolta, M. R., Bennett, C. L., Dunkley, J., Hinshaw, G., Jarosik, N., Komatsu, E., Page, L., Peiris, H. V., Verde, L., Halpern, M., Hill, R. S., Kogut, A., Limon, M., Meyer, S. S., Odegard, N., Tucker, G. S., Weiland, J. L., Wollack, E., & Wright, E. L. 2007, ApJS, 170, 377

Yesuf, H. M. 2008, Princeton University

Zakamska, N. L., Schmidt, G. D., Smith, P. S., Strauss, M. A., Krolik, J. H., Hall, P. B., Richards, G. T., Schneider, D. P., Brinkmann, J., & Szokoly, G. P. 2005, AJ, 129, 1212

Zakamska, N. L., Strauss, M. A., Heckman, T. M., Ivezić, Ž., & Krolik, J. H. 2004, AJ, 128, 1002

Zakamska, N. L., Strauss, M. A., Krolik, J. H., Collinge, M. J., Hall, P. B., Hao, L., Heckman, T. M., Ivezić, Ž., Richards, G. T., Schlegel, D. J., Schneider, D. P., Strateva, I., Vanden Berk, D. E., Anderson, S. F., & Brinkmann, J. 2003, AJ, 126, 2125